

# Mapping technique of climate fields between GCM's and ice models

T. J. Reerink, M. A. Kliphuis, and R. S. W. van de Wal

Institute for Marine and Atmospheric research Utrecht, Utrecht University, 3508 TA Utrecht, The Netherlands

Received: 29 May 2009 – Published in Geosci. Model Dev. Discuss.: 14 July 2009

Revised: 10 November 2009 – Accepted: 19 November 2009 – Published: 11 January 2010

**Abstract.** Here, we present a mapping method OBLIMAP, which projects and interpolates fields like surface temperature, surface mass balance, and surface height between a geographical based coordinate system of a General Circulation Model (GCM) and a rectangular based Ice Model (IM). We derive an oblique stereographic projection and its inverse, which holds for any area at the Earth's surface, and which can be combined with two different interpolation methods. The first one is suited to interpolate the projected fields of a coarse GCM grid on a fine meshed IM grid. The second one is appropriate for the opposite case. Both grids are allowed to be arbitrary and irregularly spaced. Therefore the OBLIMAP technique is suitable for any GCM-IM combination. After a first scan of the GCM grid coordinates and the specification of the IM grid, fast mapping of various fields is possible. To and fro (GCM-IM-GCM) mapping tests with the Climate Community System Model (CCSM) at T42 resolution ( $\sim 313$  km) and the Regional Atmospheric Climate Model (RACMO) at  $\sim 11$  km and  $\sim 55$  km, show average temperature differences of less than 0.1 K with small standard deviations. OBLIMAP, available at GMD, is an accurate, robust and well-documented mapping method for coupling an IM with a GCM or to map state of the art initial and forcing fields available at geographical coordinates to any local IM grid with an optimal centered oblique projection. Currently, the oblique stereographic and the oblique Lambert azimuthal equal-area projections for both the sphere and the ellipsoid are implemented in OBLIMAP.

prove the reliability of GCM runs; evidently on geological time scales with a highly variable ice extent, but also for scenario runs with a time horizon of only 100 years.

Quantities that are calculated by GCM's like the surface temperature and the surface mass balance, the sum of accumulation and surface melt, are the forcing of an ice sheet determining its expansion and retreat, which the other way around affect the climate system via the albedo, the surface topography, and the fresh water input in the ocean. For this reason GCM's and IM's need to be coupled. In practice this causes problems because GCM's are designed for global simulations on a coarse grid based on geographical (longitude, latitude) coordinates. Contrary, the ice dynamical equations are favorably solved on a grid with rectangular coordinates because the transformation of the ice dynamical equations to geographical coordinates introduces many extra complicating terms, in particular given the tendency of including more and more stress terms (see e.g. Pattyn, 2003; Reerink et al., 2009). Moreover calculations with a GCM are very time consuming and therefore only limited runs can be performed with a relatively coarse resolution. Typical grid sizes range from T42 ( $\sim 313$  km) to T159 ( $\sim 45$  km). The typical grid size for modeling ice sheets is about 20 km or smaller and the extent of the IM grid is not globally, but limited to ice covered areas. The typical time scale for an ice cap run is ten-thousands of years whereas most GCM runs span only a few hundred years. This mismatch in spatial and temporal scale between IM's and GCM's and the difference between their coordinate systems, demands a coupling approach in which both models are used in their own set up and in which the resulting fields have to be mapped between them (see also Rutt et al., 2009).

Hitherto in a first coupling approach ice sheet models were forced with time slice results of a GCM for near future conditions (e.g. Huybrechts et al., 2004; Van de Wal et al., 2001) or for paleo purposes (e.g. Fabre et al., 1998). This is not that critical as the mapping and projection is only done once and the IM continues to run offline. In a kind of intermediate approach DeConto and Pollard (2003) coupled a single polar ice sheet asynchronously, i.e. the results are

## 1 Introduction

Ice sheets, are often poorly resolved in General Circulation Models (GCM's). Their extent and surface height distribution are fixed or only represented by a thin ice layer. However, the complex interaction of the ice sheet with the ocean-atmosphere system demands an interactive approach to im-



Correspondence to: T. J. Reerink  
(t.reerink@uu.nl)

exchanged between the two models only once in a while. In another intermediate attempt, the climate anomalies from the GCM are used to drive a mass balance model of an ice sheet, and contrary the fresh water flux from the IM affects the ocean model (e.g. Huybrechts et al., 2002; Fichefet et al., 2003). More demanding is the direct use of (regional) climate model output to estimate the surface mass balance and the surface temperature to force the IM, and where the surface topography and other surface properties as the surface temperature and the albedo are transferred back to the GCM after each time step. An example of such a study is the work by Ridley et al. (2005) who coupled the HadCM3 model to an ice-sheet model of Greenland. They used a coarse coupling as temperatures were corrected with fixed lapse rates and ablation rates were calculated with a degree-day model. More recently Mikolajewicz et al. (2007) and Vizcaino et al. (2008) presented results of a similar approach for the ECHAM model with also schematic ablation calculations and a limited focus on the coupling technique itself.

They all use a polar stereographic projection, which is adequate for areas roughly centered around the poles. However, less centered regions like Greenland, any local part of Antarctica like the Peninsula, or the Tibetan plateau demand a local centered projection which is independent of the location, i.e. it should work for any area of interest. Besides, in a mapping strategy for the two way coupling no significant mass or energy might be lost just by the mapping, and the mapping needs to be fast. OBLIMAP suffices all those requirements.

Here we propose to use an oblique stereographic projection because it can be used for any area; equatorial, high latitude and polar. In the oblique case any area can be mapped with an optimal centered projection because any axis can be chosen as the projection axis. Whereas only the north-south pole axis can be used in the polar stereographic case. Projecting a local area at low latitude with a polar projection will unnecessarily lead to larger distortions because the projection plane cannot be centralized.

Another interesting projection in this context is the oblique Lambert equal-area projection (Snyder, 1987, p. 182) which is also available in OBLIMAP. In this manuscript we use the stereographic projection as the default to keep the structure clear, but both oblique projections are interchangeable which will be addressed only in the discussion. The stereographic projection is conformal and azimuthal (i.e. perspective), and by choosing an optimal parallel projection plane it will be close to equal-area. Conformal means that the relative local directions are true at any given point (e.g. Snyder, 1987, p. 4), which might be important from ice modeling perspective to keep a match with the ice flow directions. The Lambert azimuthal equal-area projection is equal-area and azimuthal but non conformal. Its equal-area property is interesting with respect to the mapping of conserved quantities.

We derived for both the oblique and the inverse oblique stereographic projection a single set of equations which are

successful in all eight octants (and borders) of the spherical surface, and at the poles. Also Snyder (1987, p. 154) presents equations for the oblique stereographic projection, but derivations are omitted. His equations are obtained by taking the polar projection with an additional translation to the oblique case (see Snyder, 1987, chapter 5 with its exceptions and their alternatives). Here we directly derive the oblique case by finding the points of intersection of several surface equations and parameter representations. The mapped data should be projected on well defined and well oriented grid planes (of any size and at any location) requiring this accurate and clear derivation. In case of OBLIMAP any projected IM grid has the Cartesian orientation relative to the normal vector on the spherical surface, which implies that a continuous collection of projected grid planes over the globe is obtained including the polar cases.

Because the projected grid points will not coincide with the target grid points, the projected fields have to be interpolated on the target grid. For both mapping directions OBLIMAP contains two interpolation methods: for the case of a relatively coarse and a relatively fine meshed target grid. The resolution of both model grids is not restricted, nor their grid distribution, for instance a Gaussian grid is allowed. Both interpolation methods are robust for data gaps and limited grid areas.

Comparing the initial GCM fields with their corresponding to and from (GCM-IM-GCM) mapped fields tests the OBLIMAP mapping. The differences after mapping are only due to interpolation (the projection is exact) and are small compared to the local field errors. Average differences and their standard deviations for tests with the Climate Community System Model (CCSM) and the Regional Atmospheric Climate Model (RACMO) data are presented. OBLIMAP is developed as a part of our ice model ICEDYN, but is added as a stand alone code at the GMD site (see supplementary material <http://www.geosci-model-dev.net/3/13/2010/gmd-3-13-2010-supplement.zip>) and is distributed under the terms of the GNU General Public License.

OBLIMAP is also useful for experiments in which initial fields as ice thickness and bedrock topography (Lythe et al., 2001; Bamber et al., 2001, 2009) are combined with forcing fields of a nested higher resolution regional model like RACMO (Van de Berg et al., 2006; Ettema et al., 2009). Such initial and forcing fields can be combined with an equal and optimal centered projection towards a local IM subgrid.

## 2 Method

### 2.1 Mapping method

Mapping of the GCM fields which are defined on a coarse grid with geographical coordinates towards a fine IM grid with rectangular coordinates is a sequence of projection and interpolation by distance-weighted averaging. The

coordinates of the GCM grid points are projected by an oblique stereographic projection on to a plane which coincides with the IM grid. The projected GCM grid point coordinates will in general not coincide with the IM grid point coordinates but fall in between irregularly. For each of the fine meshed IM grid points we select the nearest projected GCM grid point in each of the four quadrants around such an IM grid point. With those four nearest projected GCM grid points the resulting mapped value for this IM grid point is obtained by a Shepard distance-weighted averaging interpolation method. We call this the “quadrant method”. In case a projected point coincides with a target grid point it will dominate the weighting by adjusting its distance to 1 cm, avoiding division by zero. It depends on the GCM, but for instance for the CCSM T42 grid there are no GCM grid points within the potentially ice covered areas between  $-90^\circ \leq \phi \leq -87^\circ$  and  $87^\circ \leq \phi \leq 90^\circ$  north (with  $\phi$  the latitude), in that case the projected GCM points used for interpolation are located further away in the quadrants.

Opposite, mapping the IM fields which are defined on a fine meshed grid towards the coarse GCM grid, is also a sequence of projection and interpolation by distance-weighted averaging but within a certain radius. The coordinates of the IM grid points are projected by an inverse oblique stereographic projection on to the curved plane which coincides with the Earth's surface and the GCM grid. The projected IM grid point coordinates coincide not necessarily with the GCM grid points. In case of a relatively coarse GCM grid size all projected IM points within a radius of the order of half the GCM grid size are included by a Shepard distance-weighted averaging interpolation method to obtain a representative value for this GCM grid point. We call this the “radius method”. In this method projected points at zero distance are neglected. Because of the limited extent of the IM grid, only those GCM points within the considered area will participate in the inverse projection.

## 2.2 The oblique stereographic projection

OBLIMAP is capable of mapping any area on the Earth surface for which the middle point of interest  $M = (\lambda_M, \phi_M)$  is specified. This area is projected from the center of projection  $C$ , being the anti-pole of  $M$ , on a plane lying parallel to the tangent plane in  $M$  but some distance inward. This distance has to be specified by an angle  $\alpha$  which determines the exact stereographic projection.

First we define the used coordinate systems, thereupon we continue with a qualitative description of the oblique stereographic projection and its inverse before we present the results.

### 2.2.1 Involved coordinate systems

We use the following coordinate systems in the derivation of the projection formula's:

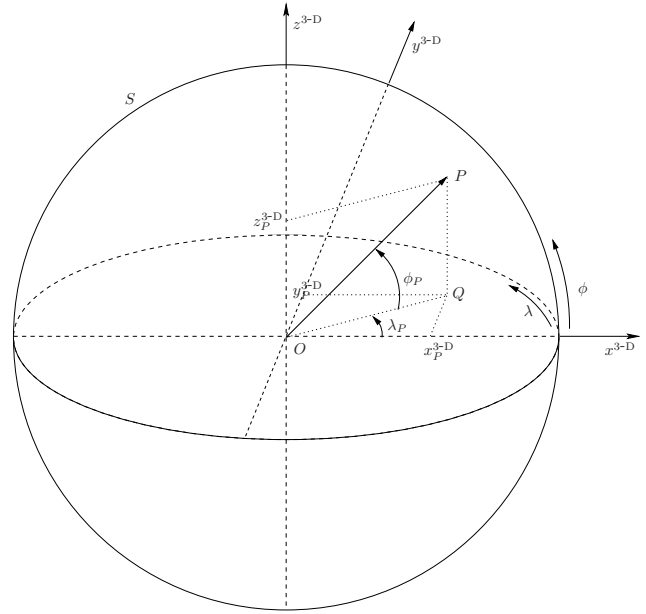


**Fig. 1.** The figure shows the axes and their orientation for the 3-D cartesian rectangular coordinate system  $(x^{3-D}, y^{3-D}, z^{3-D})$  and the 3-D spherical coordinate system  $(\lambda, \phi, r)$ . The spherical coordinate  $\lambda$  lies in the  $x^{3-D}y^{3-D}$ -plane, while the spherical coordinate  $\phi$  equals the angle  $OQP$  which lies in a plane perpendicular to this  $x^{3-D}y^{3-D}$ -plane. Above this  $x^{3-D}y^{3-D}$ -plane  $\phi$  is positive while below it  $\phi$  is negative. As in a cartesian spherical system,  $\lambda$  is chosen counter-clockwise positive and  $r$  is positive outward.  $P(\lambda + \lambda_P, \phi = \phi_P, r = R)$  is a point on the sphere  $S$  with radius  $R$ . Here  $P$  lies in the first octant in which all coordinates are positive.

- The 3-D rectangular cartesian coordinate system:  $(x^{3-D}, y^{3-D}, z^{3-D})$ , with  $x^{3-D}, y^{3-D}, z^{3-D} \in \mathbb{R}$  and with the origin  $O = (x^{3-D}=0, y^{3-D}=0, z^{3-D}=0)$ . See Fig. 1.
- The 3-D spherical coordinate system:  $(\lambda, \phi, r)$ , with  $0^\circ \leq \lambda \leq 360^\circ$  and with the origin  $O = (\lambda, \phi, r=0)$ , which coincides with the origin  $O$  of the 3-D rectangular cartesian coordinate system. See Fig. 1.
- The 2-D rectangular cartesian coordinate system:  $(x_{IM}, y_{IM})$ , with  $x_{IM}, y_{IM} \in \mathbb{R}$  where we define the origin  $M' = (x_{IM}=0, y_{IM}=0)$ . The plane spanned by  $x_{IM}$  and  $y_{IM}$  is called  $S'$ . In the 3-D spherical coordinate system the coordinates of the origin  $M'$  are  $M' = (\lambda_M, \phi_M, R \cos \alpha)$ . The IM grid points are points in this 2-D rectangular cartesian coordinate system. See the red colored plane in Fig. 2.
- The 2-D geographical longitude-latitude coordinate system defined on the Earth's surface:  $(lon, lat)$  with  $0^\circ \leq lon \leq 360^\circ$  and  $-90^\circ \leq lat \leq 90^\circ$ . The curved spherical plane representing the surface of the Earth is defined as  $S$ . In the 3-D spherical coordinate system these 2-D  $(lon, lat)$  coordinates can be described with  $(\lambda, \phi, r) = (\lambda, \phi, R)$  with  $R$  the radius (in m) of  $S$  and the Earth.

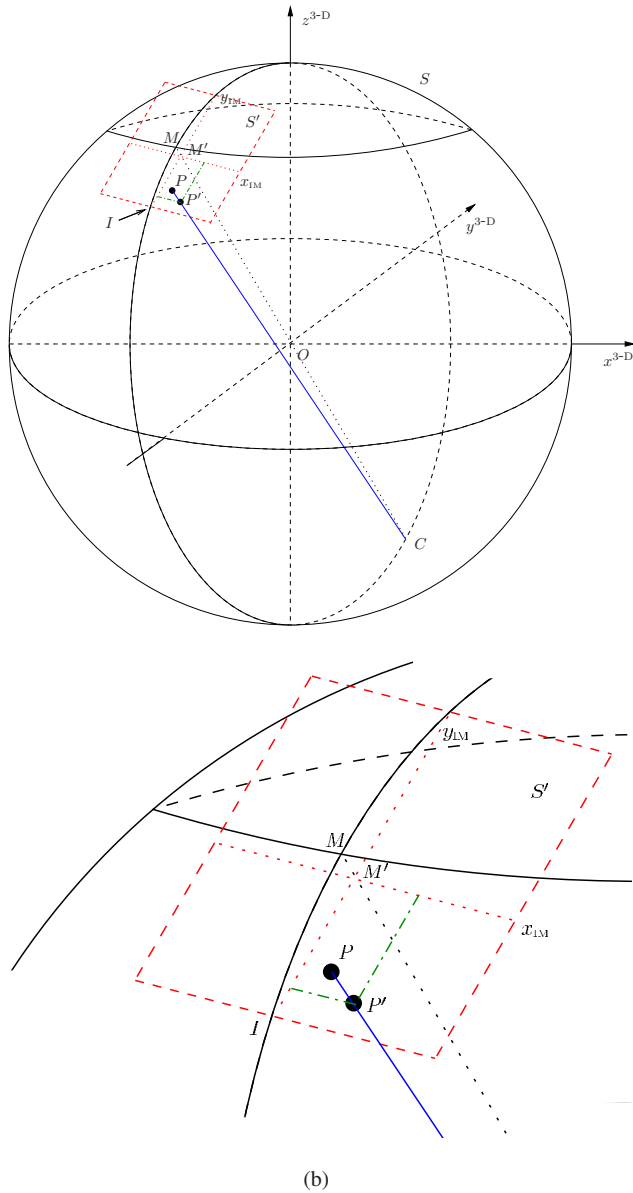


**Fig. 2.** Figure (a) shows a GCM point  $P$  on  $S$  which is projected on  $S'$  along the line  $\overrightarrow{CP}$ . The projected point  $P'$  is situated in plane  $S'$  which coincides with the red colored IM grid. The coordinates of  $P'$  in the IM grid which coincides with  $S'$  are indicated by the components (in green) relative to the IM axes. The global GCM grid coincides with the spheric surface  $S$ . The IM is a regional model and therefore has a relatively small extent, see the red colored IM grid. Note that a relatively small IM grid is sketched, with a well chosen  $\alpha$  the horizontal extent will be larger than the  $M'I$  drawn here. Figure (b) shows a close up of the projection plane.

In fact these angle coordinates equal the (*lon*, *lat*) coordinates, so  $lon=\lambda$  and  $lat=\phi$ . The GCM grid is based on these coordinates, see the  $\lambda$  and  $\phi$  in Fig. 1 in case  $r=R$ .

Figure 1 illustrates the relation between both 3-D systems, and Fig. 2 illustrates the location of the plane  $S'$  in the 3-D rectangular coordinate system. For the 2-D geographical and the 3-D spherical coordinate systems the value of the longitude  $\lambda$  is undetermined at the North Pole (NP) and at the South Pole (SP).

## 2.2.2 Description of the projection

In an oblique stereographic projection the points from a spherical surface  $S$  are projected to a rectangular plane  $S'$ , see Fig. 2 for the projection of a single point  $P$ . This spherical surface  $S$  is part of a sphere with radius  $R$ . In our case the GCM grid points are points on  $S$  and the IM grid points are points on  $S'$ . Roughly the oblique stereographic projection can be described as follows: Consider a specified point  $M=(\lambda_M, \phi_M, R)$  in the middle of an area of interest on  $S$ . The center of projection  $C$  is the anti-pole of  $M$ , it lies on  $S$  but just at the opposite side of  $S$ . An arbitrary point  $P$  on  $S$  will be projected along the line  $\overrightarrow{CP}$  into the plane  $S'$ , see Fig. 2. Usually  $P$  is a point not too far from  $M$ . The projected point  $P'$  is the point of intersection of the line  $\overrightarrow{CP}$  and the plane  $S'$ . The plane  $S'$  is parallel to the plane which is tangent to the sphere  $S$  in point  $M$ , and therefore perpendicular to  $\overrightarrow{CM}$  as well. The exact location of  $S'$  (along  $\overrightarrow{CM}$ ) depends on the place of intersection of  $S'$  with  $S$ . If  $I$  is this point of intersection of  $S'$  with  $S$ , then  $\alpha$  is the angle  $MOI$  which determines the exact stereographic projection, see Fig. 3. Often the complement angle  $\beta$  of  $\alpha$  is used to specify the stereographic projection:  $\beta=90^\circ-\alpha$ .  $M'$  is the point of intersection of  $\overrightarrow{CM}$  (or  $\overrightarrow{OM}$ ) and  $S'$ , and will be the origin of the 2-D rectangular coordinates  $x_{IM}$  and  $y_{IM}$  of the IM grid which coincides with the plane  $S'$ . The extent of the IM grid  $x_{IM}^{\min}, x_{IM}^{\max}, y_{IM}^{\min}$  and  $y_{IM}^{\max}$  of  $S'$  have to be specified, in OBLIMAP in terms of the grid sizes and the grid spacings.

At the intersection circle of  $S$  and  $S'$ , distances are projected one to one. While distances on  $S$  at the  $M$  side of  $S'$  shrink and distances on  $S$  at the  $O$  side enlarge, see Fig. 3. Therefore an optimal  $\alpha$  leads on average to a one to one projection (or close to that in case an asymmetric region requires a non-squared grid) in the area of interest. A reasonable  $\alpha$  can be estimated by requiring that half the IM grid area falls inside the intersection circle with radius  $M'I$ :

$$\pi(M'I)^2 = \frac{1}{2} N_x N_y \Delta x \Delta y \quad (2.1)$$

with  $N_x, N_y, \Delta x$ , and  $\Delta y$  the number of grid points and the grid spacing in  $x$ - and  $y$ -direction.

Then, from Fig. 3 one can immediately derive that for a grid with  $N_x N_y \Delta x \Delta y \leq 2\pi R^2$  an optimal  $\alpha$  equals

$$\alpha = \arcsin \left( \frac{1}{R} \sqrt{\frac{1}{2\pi} N_x N_y \Delta x \Delta y} \right) \quad (2.2)$$

With the red colored IM grid in Fig. 2 at the correct position and with  $\alpha$  as in Eq. (2.2), an optimal projection is obtained.

For Antarctica often  $\alpha=19^\circ$  is chosen, and for Greenland, because it is smaller, a lower  $\alpha$  will be better.

If Antarctica is the area of interest we choose  $M$  equal to the SP. In that case the projection is called a polar stereographic projection for which our formula's hold as well. The stereographic projection is called oblique if the axis  $\overrightarrow{CM}$  can be any axis, so  $M$  can be any point on  $S$ . E.g. in case of Greenland, we take  $M = (\lambda_M=320^\circ, \phi_M=72^\circ)$ .

To summarize: the distance  $\overrightarrow{MM'}$  is controlled by specifying  $\alpha$  which determines the exact oblique stereographic projection. The area of interest is chosen by specifying  $M(\lambda_M, \phi_M)$  and the IM grid extents  $x_{IM}^{\min}, x_{IM}^{\max}, y_{IM}^{\min}$  and  $y_{IM}^{\max}$ .

### 2.2.3 The oblique stereographic projection

The longitude-latitude coordinates  $\lambda_P$  and  $\phi_P$  of an arbitrary point  $P$  on the spherical surface  $S$  are projected to a rectangular plane  $S'$  which coincides with the IM grid with origin  $M'$ . After specifying  $\lambda_M$  and  $\phi_M$ , the coordinates  $x_{IM_{P'}}$  and  $y_{IM_{P'}}$  of the projected point  $P'$  relative to the IM grid can be calculated. Under the condition

$$\lambda_M = 0^\circ \quad \text{for} \quad \phi_M = -90^\circ \quad \& \quad \phi_M = 90^\circ \quad (2.3)$$

the final result for the oblique stereographic projection is

$$x_{IM_{P'}} = R(\cos\phi_P \sin(\lambda_P - \lambda_M))t_{P'} \quad (2.4)$$

$$y_{IM_{P'}} = R[\sin\phi_P \cos\phi_M - (\cos\phi_P \sin\phi_M) \cos(\lambda_P - \lambda_M)]t_{P'} \quad (2.5)$$

with

$$t_{P'} = \frac{1 + \cos\alpha}{1 + \cos\phi_P \cos\phi_M \cos(\lambda_P - \lambda_M) + \sin\phi_P \sin\phi_M} \quad (2.6)$$

which is derived in Appendix A. The angles are in degrees and the distances in m.

### 2.2.4 The inverse oblique stereographic projection

The final result for the inverse oblique stereographic projection for an arbitrary point  $P'$  in  $S'$  to  $P$  in  $S$ , is given by

$$\left. \begin{aligned} \lambda_P &= 180^\circ + \frac{180}{\pi} \arctan \frac{y_{P'}^{3-D}}{x_{P'}^{3-D}} && x_{P'}^{3-D} < 0 \\ \lambda_P &= \frac{180}{\pi} \arctan \frac{y_{P'}^{3-D}}{x_{P'}^{3-D}} && x_{P'}^{3-D} > 0 \quad \& \quad y_{P'}^{3-D} \geq 0 \\ \lambda_P &= 360^\circ + \frac{180}{\pi} \arctan \frac{y_{P'}^{3-D}}{x_{P'}^{3-D}} && x_{P'}^{3-D} > 0 \quad \& \quad y_{P'}^{3-D} < 0 \\ \lambda_P &= 90^\circ && x_{P'}^{3-D} = 0 \quad \& \quad y_{P'}^{3-D} > 0 \\ \lambda_P &= 270^\circ && x_{P'}^{3-D} = 0 \quad \& \quad y_{P'}^{3-D} < 0 \\ \lambda_P &= 0^\circ && x_{P'}^{3-D} = 0 \quad \& \quad y_{P'}^{3-D} = 0 \end{aligned} \right\} \text{for} \quad (2.7)$$

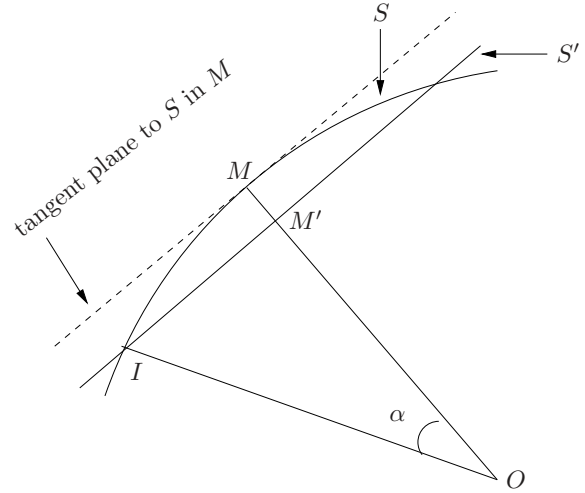


**Fig. 3.** This cross section shows how the position of the plane  $S'$  is determined by  $\alpha$ .  $S'$  is parallel to the plane which is tangent to the sphere  $S$  in point  $M$  and  $S'$  is shifted a certain distance  $MM'$  along  $\overrightarrow{OM}$ . This distance is determined by the intersection point  $I$  which is controlled by  $\alpha$ . The choice of  $\alpha$  thus determines the distance  $MM'$ .

and

$$\left. \begin{aligned} \phi_P &= \frac{180}{\pi} \arctan \frac{z_{P'}^{3-D}}{\sqrt{x_{P'}^{3-D^2} + y_{P'}^{3-D^2}}} && x_{P'}^{3-D} \neq 0 \quad \text{or} \quad y_{P'}^{3-D} \neq 0 \\ \phi_P &= 90^\circ && \text{for} \quad x_{P'}^{3-D} = y_{P'}^{3-D} = 0 \quad \& \quad z_{P'}^{3-D} > 0 \\ \phi_P &= -90^\circ && x_{P'}^{3-D} = y_{P'}^{3-D} = 0 \quad \& \quad z_{P'}^{3-D} < 0 \end{aligned} \right\} \quad (2.8)$$

with

$$x_P^{3-D} = R(\cos\lambda_M \cos\phi_M)(t_P - 1) + x_{P'}^{3-D}t_P \quad (2.9)$$

$$y_P^{3-D} = R(\sin\lambda_M \cos\phi_M)(t_P - 1) + y_{P'}^{3-D}t_P \quad (2.10)$$

$$z_P^{3-D} = R(\sin\phi_M)(t_P - 1) + z_{P'}^{3-D}t_P \quad (2.11)$$

in which

$$t_P = \frac{2R^2 + 2Ra}{R^2 + 2Ra + (x_{P'}^{3-D})^2 + (y_{P'}^{3-D})^2 + (z_{P'}^{3-D})^2} \quad (2.12)$$

in which

$$a = (\cos\lambda_M \cos\phi_M)x_{P'}^{3-D} + (\sin\lambda_M \cos\phi_M)y_{P'}^{3-D} + (\sin\phi_M)z_{P'}^{3-D} \quad (2.13)$$

and

$$x_{P'}^{3-D} = R\cos\alpha \cos\lambda_M \cos\phi_M - (\sin\lambda_M)x_{IM_{P'}} - (\cos\lambda_M \sin\phi_M)y_{IM_{P'}} \quad (2.14)$$

$$y_{P'}^{3-D} = R\cos\alpha \sin\lambda_M \cos\phi_M + (\cos\lambda_M)x_{IM_{P'}} - (\sin\lambda_M \sin\phi_M)y_{IM_{P'}} \quad (2.15)$$

$$z_{P'}^{3-D} = R\cos\alpha \sin\phi_M + (\cos\phi_M)y_{IM_{P'}} \quad (2.16)$$

which is derived in Appendix B. The angles are in degrees and the distances in m.

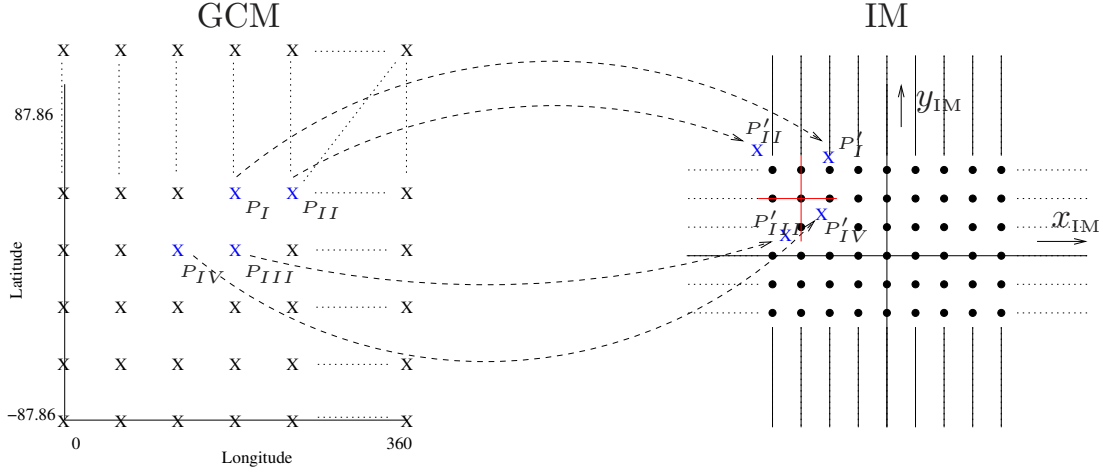


**Fig. 4.** The figure illustrates the interpolation: through each grid point  $(x_{\text{IM}}(m), y_{\text{IM}}(n))$  we draw an imaginary cross (red cross) that divides the area around the grid point into four quadrants. Then in each quadrant we determine the projected GCM grid point that lies closest to  $x_{\text{IM}}(m), y_{\text{IM}}(n)$  (blue crosses). Those points we call  $P'_I, P'_{II}, P'_{III}$  and  $P'_{IV}$ .

### 2.3 Interpolation of the projected fields

With the formula's presented in Sect. 2.2.3 and 2.2.4 we can project any GCM grid point  $(\lambda, \phi)$  towards an IM grid  $(x_{\text{IM}}, y_{\text{IM}})$ , and vice versa. Suppose we want to map a two-dimensional GCM field ( $F_{\text{gcm}}^{2-D}$ ) to the IM grid, then the projected points will in general not coincide with the IM grid points. Therefore we determine the mapped two-dimensional IM field ( $F_{\text{im}}^{2-D}$ ) values at the IM grid by interpolation of the projected GCM points in the surrounding quadrants. In the opposite map direction, we determine the  $F_{\text{gcm}}^{2-D}$  values at the GCM grid by averaging all projected IM grid points within a certain radius, where each projected IM grid point contributes depending on its distance to the considered GCM point.

#### 2.3.1 Interpolation on to the IM grid of a projected GCM field: quadrant method

Let  $i$  and  $j$  be the longitudinal and latitudinal grid indices for the GCM grid and  $P_{ij}=(\lambda(i), \phi(j))$  a point at the GCM grid. Furthermore, let  $m$  and  $n$  be the  $x_{\text{IM}}$  and  $y_{\text{IM}}$  grid indices for the IM grid. Then corresponding to  $P_{ij}$ ,  $P'_{ij}$  is the projected point relative to the IM coordinate system and will in general not coincide with an IM grid point but fall in between, see the blue crosses in Fig. 4. To obtain the values of the  $F_{\text{im}}^{2-D}$  field at the IM grid points  $(x_{\text{IM}}(m), y_{\text{IM}}(n))$ , the  $F_{\text{gcm}}^{2-D}$  field values of the nearest  $P'_{ij}$  points are interpolated. Since these  $P'_{ij}$  do not lie in an equidistant manner around  $(x_{\text{IM}}(m), y_{\text{IM}}(n))$  we use a quadrant method based on the Shepard interpolation technique (Shepard, 1968).

In Fig. 4 an imaginary cross positioned at each IM grid point  $(x_{\text{IM}}(m), y_{\text{IM}}(n))$  divides the area around the grid point into four quadrants. For each  $m, n$  combination we determine in each quadrant the closest  $P'_{ij}$  to  $(x_{\text{IM}}(m), y_{\text{IM}}(n))$ . Figure 4 demonstrates an example with  $P'_I, P'_{II}, P'_{III}$  and  $P'_{IV}$  being the nearest IM grid points to the red cross.

Let  $d_I, d_{II}, d_{III}$  and  $d_{IV}$  be the Euclidian distance for the four quadrants respectively from each of these points to the considered IM grid point  $(x_{\text{IM}}(m), y_{\text{IM}}(n))$ , then the formula for the Shepard distance-weighted averaging interpolation becomes:

$$F_{\text{im}}^{2-D}(x_{\text{IM}}(m), y_{\text{IM}}(n)) = \frac{\sum_{q=I}^{IV} \frac{F_{\text{gcm}}^{2-D}(P_q)}{(d_q)^e}}{\sum_{q=I}^{IV} \frac{1}{(d_q)^e}} \quad (2.17)$$

where  $q$  counts over the four quadrants  $I, II, III$ , and  $IV$ ,  $P_q$  is the nearest projected GCM grid point in quadrant  $q$  at a distance  $d_q$  relative to the considered IM grid point  $(m, n)$ , and  $e$  is the distance weighting exponent, usually  $e=2$  is considered to be the fairest choice for this type of problems (Shepard, 1968).

#### 2.3.2 Interpolation on to the GCM grid of a projected IM field: radius method

In this case the  $P'_{mn}$  points coincide with the IM grid points, and the corresponding projected points  $P_{mn}$  will in general not coincide with the GCM grid points  $(\lambda(i), \phi(j))$ . Because the  $P_{mn}$  will not lie in an equidistant manner around  $(\lambda(i), \phi(j))$ , and because in this case the large GCM grid should represent the many fine IM grid points in that area,

the radius method is used. This is similar to the Shepard interpolation (Shepard, 1968) for a radius  $R_s$  of about half the GCM grid size. The distance  $d_{mn}(i, j)$  of a point  $P_{mn}$  to the point  $P_{ij}$  at  $(\lambda(i), \phi(j))$  is the shortest path over the spherical surface  $S$  along a great circle:

$$d_{mn}(i, j) = R \arccos \left[ \cos(\phi_{P_{mn}}) \cos(\phi_{P_{ij}}) \cos(\phi_{P_{mn}} - \phi_{P_{ij}}) + \sin(\phi_{P_{mn}}) \sin(\phi_{P_{ij}}) \right] \quad (2.18)$$

Weighting all projected IM points within a radius  $R_s$  using the Shepard distance-weighted method, yields:

$$F_{\text{gcm}}^{2-D}(\lambda(i), \phi(j)) = \frac{\sum_{d_{mn}(i, j) \leq R_s} \frac{F_{\text{im}}^{2-D}(P_{mn})}{d_{mn}(i, j)^e}}{\sum_{d(i, j) \leq R_s} \frac{1}{d_{mn}(i, j)^e}} \quad (2.19)$$

To treat the GCM points at the edge of the IM grid correctly, the IM grid is extended with the grid edge values.

### 3 Model specifications

#### 3.1 The CCSM model

The Community Climate System Model (CCSM, see <http://www.cesm.ucar.edu>), designed by NCAR is a GCM with four separate model components simulating the Earth's atmosphere, ocean, land surface, and sea-ice which are coupled by a central coupler component. We are mostly interested in the fields from the CCSM3 atmosphere component for realistic OBLIMAP mapping tests.

The CCSM3 atmosphere fields are defined on a regular longitude-latitude T42 grid with  $128 \times 64$  grid points, see Fig. 5. It has a horizontal resolution of  $2.8^\circ$ . The grid almost covers the complete globe but the latitude is restricted between  $-87^\circ$  and  $+87^\circ$  north. Data output are in netcdf format. We used the December–February averages of the last five years of a present day control run. The results of this control run agree with Collins et al. (2005).

For the surface height we used the surface geopotential (PHIS) from CCSM. The CCSM surface temperature (TS) is the temperature of the Earth's surface at this surface geopotential. For the surface mass balance we added two CCSM components: the convective snow rate (PRECS) and the large-scale snow rate (PRECSL). We left out the evaporation and the runoff in the CCSM cases because these fields are only available in the CCSM land files for the land mask. And the complications to extend these fields are not in proportion to our goal of just providing realistic fields for our test cases.

#### 3.2 The RACMO model

The Regional Climate Model (RACMO2 van Meijgaard et al., 2009) has been used to obtain best estimates for present day atmospheric fields using model physics and all available

observations. Here, we use the surface temperature and surface mass balance resulting from the regional run for Antarctica with RACMO2/ANT (Van de Berg et al., 2006) and from the regional run for Greenland with RACMO2/GR (Ettema et al., 2009). The RACMO2/ANT data is defined on a reduced gaussian grid with  $134 \times 122$  grid points and a resolution of approximately 55 km. RACMO2/GR data is defined on a reduced gaussian grid with  $246 \times 312$  grid points and a resolution of approximately 11 km, and covers  $9.44 \cdot 10^{12} \text{ m}^2$  in total.

The RACMO surface mass balance fields are masked to the ice covered area because the runoff is only calculated there. We estimated the surface mass balance of the majority of the non ice covered points by summing the precipitation and the evaporation and subtracting 800 mm water equivalent runoff per year, but the surface mass balance for points close to the ice margin are estimated with help of the ice masked points in a short radius by a Shepard distance weighting to provide a better local estimate.

#### 3.3 The ICEDYN model

The ICEDYN model, developed at IMAU-Utrecht, is a so called 3-D thermomechanical ice model which is suited to simulate large ice caps like Antarctica and Greenland or smaller glacier systems over hundred thousands of years. The current ICEDYN revision is rather flexible by using a configuration file in which all grid specifications and time stepping choices can be specified. Choices for proper local forcings as surface temperature and surface mass balance can be specified in this configuration file, and new ones can easily be added in the current modular set up of ICEDYN. By default a 3-D thermomechanical ice-sheet is coupled with a 2-D ice-shelf, but also a simple shelfless shallow ice approximation (SIA) computation is optional from the configuration file. Both input and output of ICEDYN are in netcdf format. ICEDYN performs well against the EISMINT benchmark experiments (Huybrechts et al., 1996; Payne et al., 2000), which can be repeated by just using the EISMINT configuration file.

Depending on the experimental set up, the ICEDYN model is capable of modeling each ice cap for which certain initial and reference fields are available, and for which the forcing is known. OBLIMAP is developed as a part of ICEDYN and has a similar flexible grid specification from a configuration file. Using ICEDYN is convenient to test the OBLIMAP mapping for many grid configurations. The coordinates of the ICEDYN grid points are rectangular cartesian coordinates like the IM grid points in OBLIMAP.

The ICEDYN fields are defined on a rectangular  $(x_{\text{IM}}, y_{\text{IM}})$  grid. An example is shown in Fig. 6 with  $281 \times 281$  grid points. In this case the default horizontal resolution in  $x$ - and  $y$ -direction is 20 km and represents Antarctica with a limited area of  $5600 \text{ km} \times 5600 \text{ km}$ .

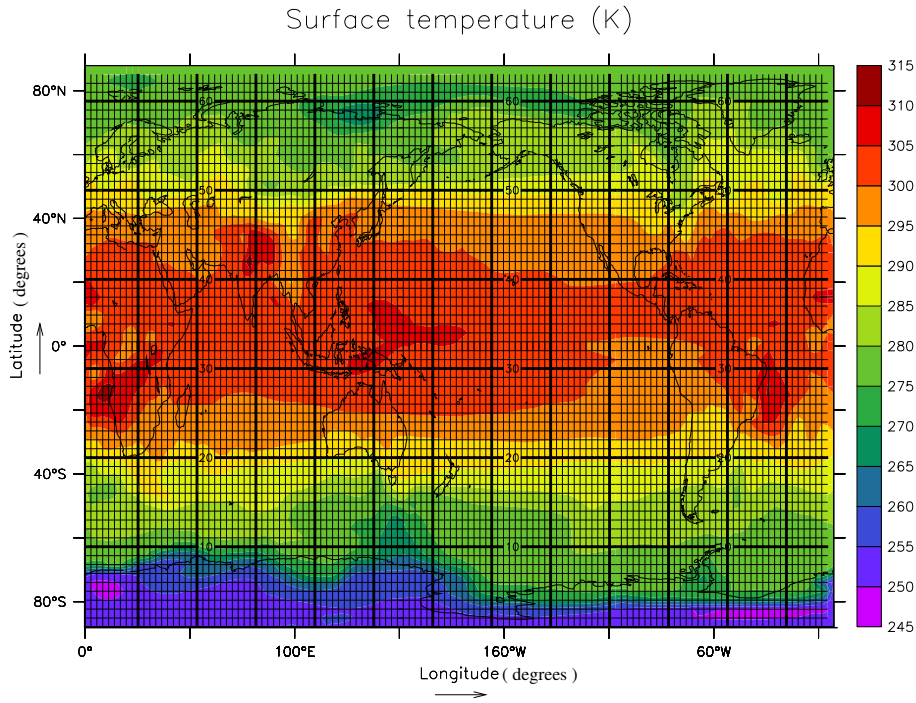


**Fig. 5.** The figure shows a global image of the surface temperature field between  $-87^\circ$  and  $+87^\circ$  north (the color scale is in Kelvin). On top, in black, the CCSM grid of the atmosphere component at T42 resolution is shown.

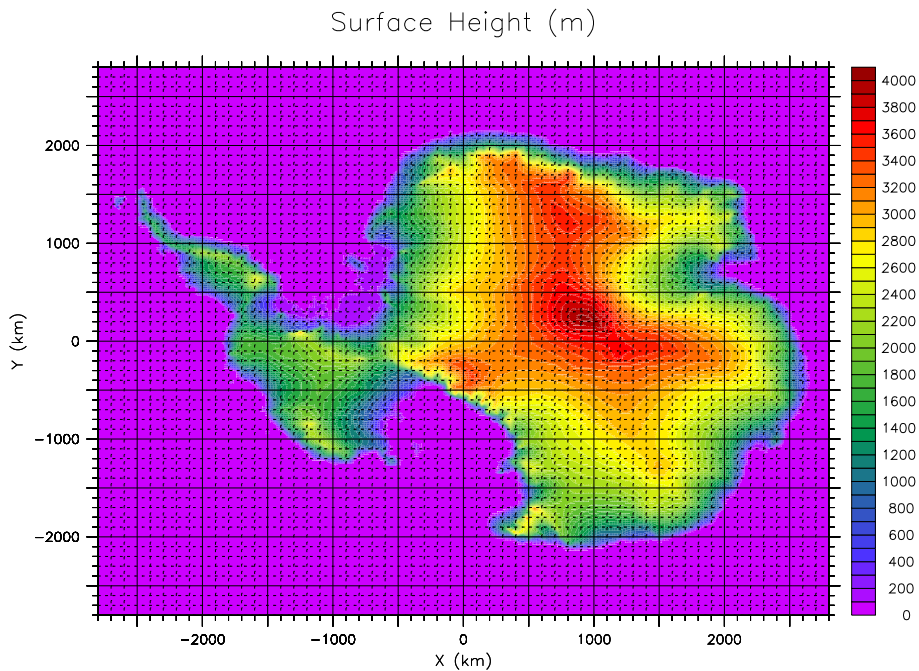


**Fig. 6.** The figure shows an image of the surface height of Antarctica (the color scale is in meter). On top, in black, the relatively fine IM grid is shown, which is in reality five times finer with a grid spacing of 20 km. The origin of the IM grid  $M'(x_{IM}(m=141)=0, y_{IM}(n=141)=0)$  represents the South Pole, where  $m$  and  $n$  are the IM grid numbers in the  $x$ - and  $y$ -direction, respectively.



#### 4 Mapping experiments

Several realistic mapping experiments with CCSM and RACMO data will demonstrate the performance of OBLIMAP. Each experiment concerns a particular area and GCM data set of interest for which the surface temperature ( $T_s$ ), the surface mass balance ( $MB$ ), and the surface height ( $H_s$ ) will be mapped to and fro. The deviations between these to and fro mapped 2-D fields and the initial field will be used to quantify the performance of the mapping.

Grid point coordinates which are to and fro projected with the oblique stereographic projection and its inverse remain identical, which means the projection is exact. However, projected points have to be interpolated on the target grid, this causes deviations after to and fro mapping. These deviations evidently increase in case the resolution of the IM and the GCM differs. Therefore, in our experiments we start with the fields of the coarse GCM to prevent interfering deviations which are not due to the mapping technique itself.

In most situations we use the quadrant method to interpolate. But in case the target grid resolution is about four or more times coarser the radius method is used, representing a better estimate of the many fine gridded points within each single coarse target grid point. After IM-GCM mapping, the mapped field values of the limited IM area are merged with those initial GCM field values which are not involved in the mapping. Averages and standard deviations ( $\sigma$ ) are calculated over the involved mapped points only.

Fourteen miscellaneous experiments show the accuracy and the robustness of the OBLIMAP mapping for two different types of GCM data (Sect. 3.1 and 3.2). These fourteen experiments and their specifications are listed in Table 1, the abbreviations of the data sets are explained in Table 2. Figures 7–14 show the results of a number of these experiments representing tests with: three GCM data sets (differing in resolution, in grid distribution, and in global extent), areas covering data gaps (e.g. Antarctica), areas at the border of the GCM domain (e.g. Ellesmere), areas with complicated patterns because of the topography (e.g. Ellesmere), local areas being part of a larger (glaciated) system (e.g. Jakobshavn), areas covering the Greenwich longitude (e.g. Svalbard), different amount of involved mapped points (e.g. Greenland versus Peninsula), different IM extents, and a spread of oblique locations.

The deviation field is the to and fro mapped GCM field minus the initial GCM field. The average mapped deviation (AMD) is the mean absolute error (MAE) of this deviation field, and is presented in Table 3 together with the  $2\sigma$  confidence interval. In addition the field range and the field average are shown in Table 3 to judge these AMD and  $2\sigma$  intervals. For several of the experiments we show in Figs. 7–14 the initial GCM field, the deviation field, and the mapped IM field for  $T_s$ ,  $MB$ , and  $H_s$ . The to and fro mapped GCM fields are omitted because they look identical, as a result of the accurate mapping. At the bottom of these figures the distribu-

tions of the deviations for  $T_s$ ,  $MB$ , and  $H_s$  are shown, where we sampled the full deviation range in 300 intervals. Most of them are sharply peaked around zero, indicating that the majority of the deviations are quite small. Although these distributions are not normal, their  $2\sigma$  interval represents about 95% confidence. Points falling within  $1\sigma$  and  $2\sigma$  are plotted blue to visualize the confidence intervals.

If necessary OBLIMAP is capable of converting the units of  $T_s$ ,  $MB$ , and  $H_s$  respectively to Kelvin, meter ice equivalent (mieq) per year (using an ice density of  $910 \text{ kg m}^{-3}$ ), and meter, for the IM. In the tables and the figures all results including the GCM ones are presented in these IM units.

In experiments 1–3 the fields are mapped between CCSM and ICEDYN, for the results see Table 3. Because in these experiments the CCSM grid is coarse compared to the ICEDYN grid we used for the ICEDYN-CCSM mapping the radius method with  $R_s \sim 125 \text{ km}$ , which is 0.8 times half the CCSM grid diameter. We multiplied by a factor 0.8 to ensure we include only points within each grid cell itself, because the grid sizes differ slightly per latitude, whereas  $R_s$  is taken constant in the current version of OBLIMAP. In Figs. 7 and 8 we show the results for Antarctica and Greenland, note that the low number of involved points for Greenland is reflected in the distribution plots. A lack of CCSM data between  $-90^\circ$  and  $-87^\circ$  complicates the mapping for Antarctica, however with our quadrant interpolation method we obtain realistic results of the south pole area for ICEDYN.

The higher RACMO resolution allows mapping tests on fields with sharper contours and larger gradients. Experiments 4–11 map the RACMO/GR data set RG2 and experiments 12–14 map the RACMO/ANT data set RA, or parts of them. For the results see Table 3. In experiment 4, see Fig. 9, the IM grid covers Greenland entirely with a 10 km resolution. While in experiments 5–8, see Figs. 10–12, and in experiments 9–11 grids with a resolution of a few kilometer are used to map local areas. Experiment 12, see Fig. 13, concerns Antarctica entirely. While experiment 13, see Fig. 14, and experiment 14 show a local mapping case of this RA data set. The difference in grid resolution is that large for the ICEDYN-RACMO mapping that we used a radius interpolation method with  $R_s \sim 4.4 \text{ km}$  for experiments 5–11, and with  $\sim 22 \text{ km}$  for experiments 13–14 (see Table 1).

In general we see for all the experiments (Figs. 7–14) that the range and pattern of the mapped IM field are in very good agreement with the initial GCM fields. And as mentioned before, after to and fro mapping the GCM fields look identical. From Table 3 and Figs. 7–14 we see for various grids for different locations a maximum AMD of 0.1 K for  $T_s$ . The AMD for  $H_s$  is about a few meter for these data. The AMD for  $MB$  varies between one millimeter and a centimeter ice equivalent per year, depending on the range of  $MB$ . The interpretation of the deviations of a field with a relatively wide range around zero (like the  $MB$ ) is more complicated because of the difference in relative deviations. In these cases the range relative deviation (RRD), equal to the percentage of

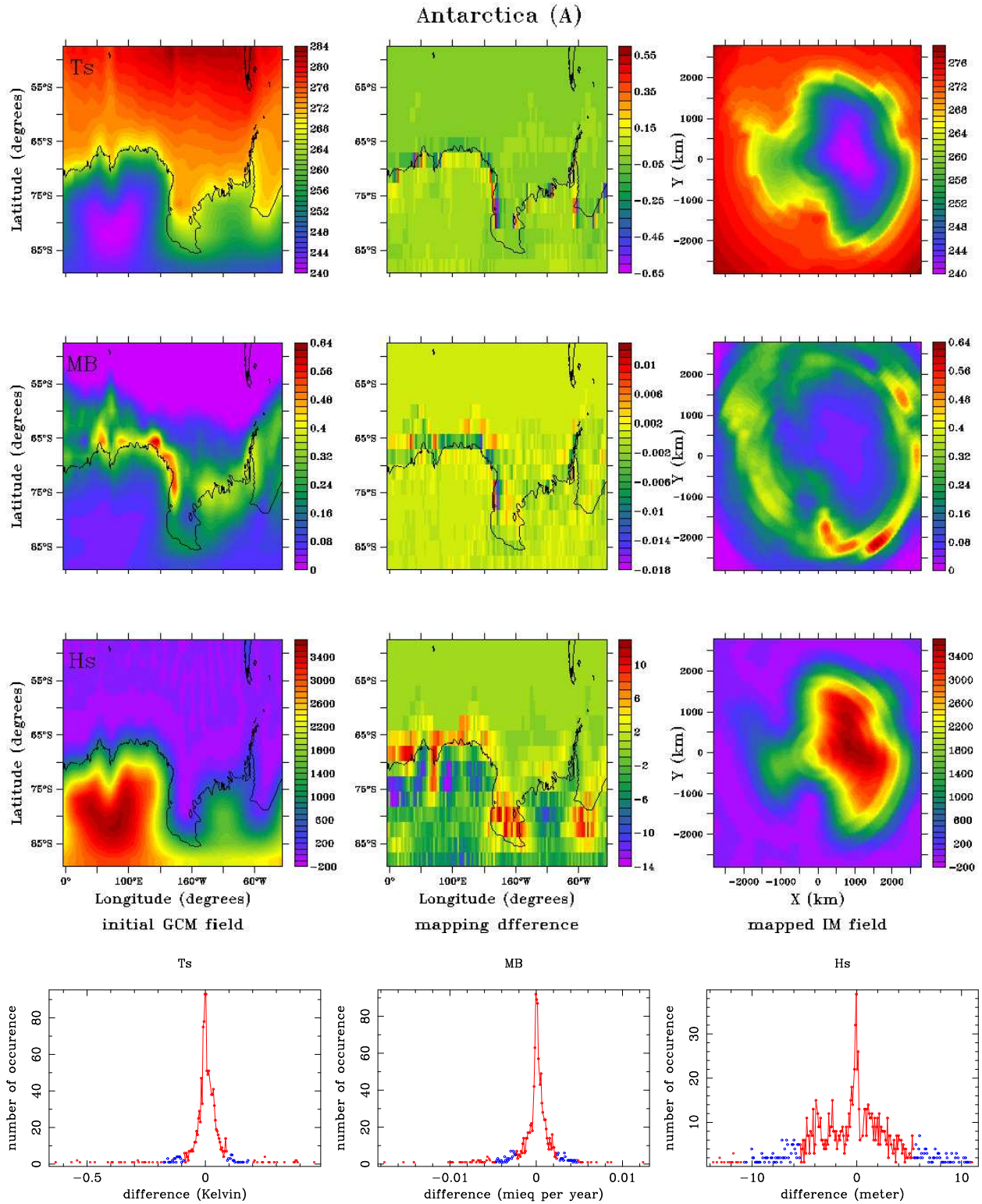


**Fig. 7.** The figure shows top-down for Antarctica (data set A) the initial GCM fields (left panels), the mapped IM fields (right panels) and the differences in the GCM fields after to and fro mapping (central panels) for  $T_s$ , MB,  $H_s$ , and the distributions of those differences after to and fro mapping. The surface temperature  $T_s$  (in Kelvin), the surface height  $H_s$  (in m), and the surface mass balance MB (in mieq per year) are indicated by the color bars left of each field panel. For convenience the points in the distribution graphs between  $1\sigma$  and  $2\sigma$  are plotted blue, and the points within  $1\sigma$  are connected by a spline.

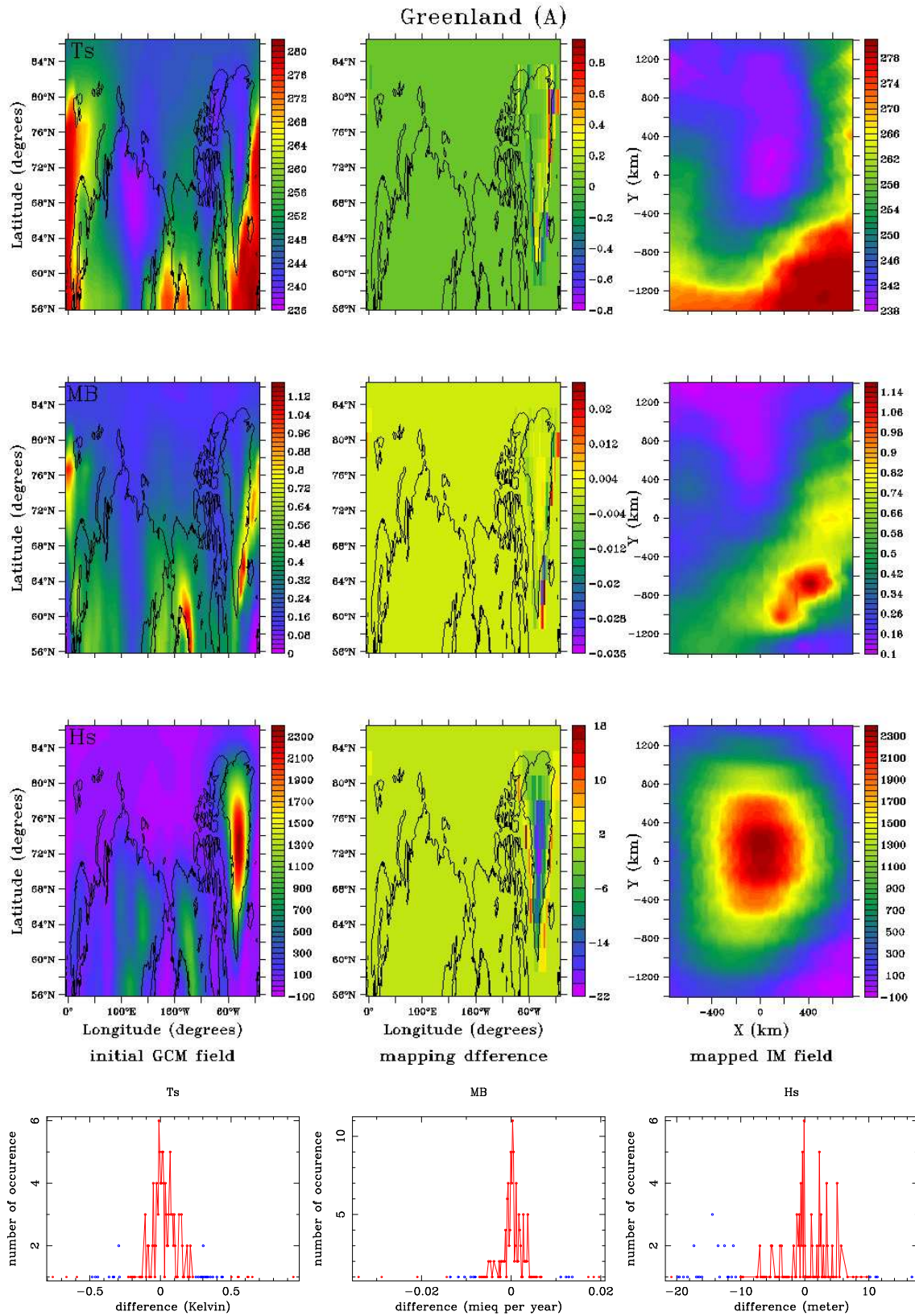


**Fig. 8.** This figure concerns Greenland (data set A), see further the caption of Fig. 7.

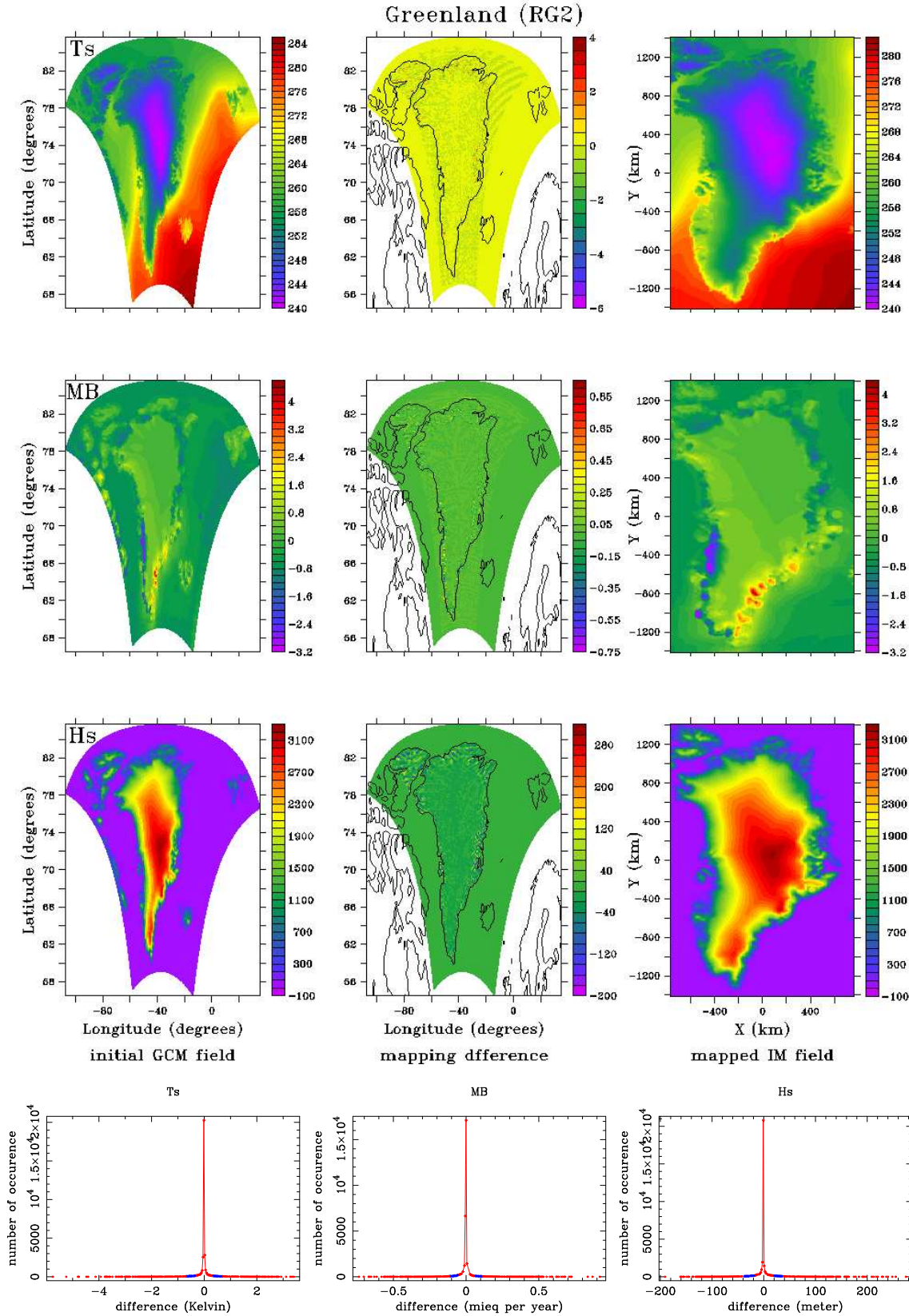


**Fig. 9.** This figure concerns Greenland (data set RG2), see further the caption of Fig. 7.

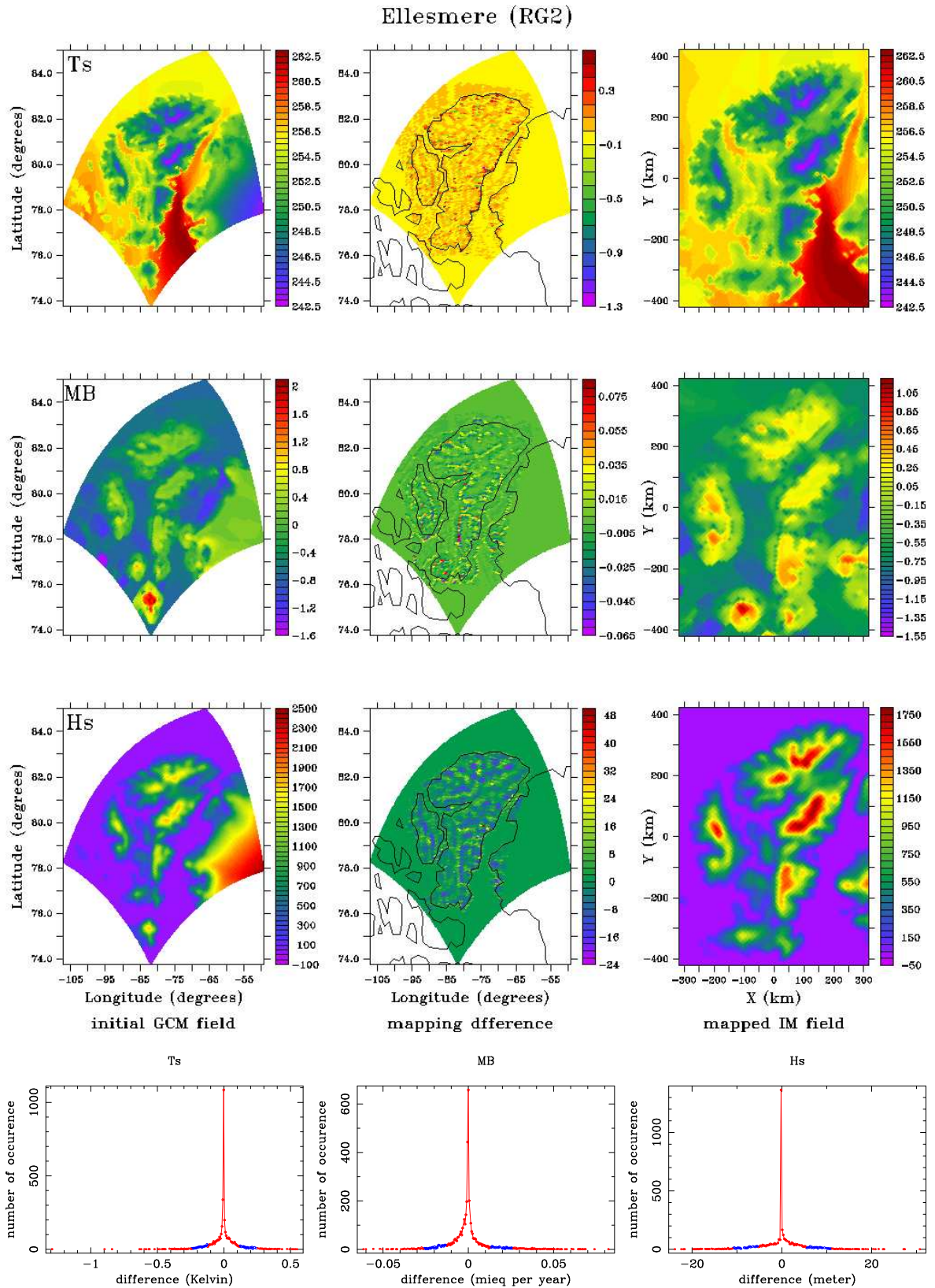


**Fig. 10.** This figure concerns Ellesmere (data set RG2), see further the caption of Fig. 7.

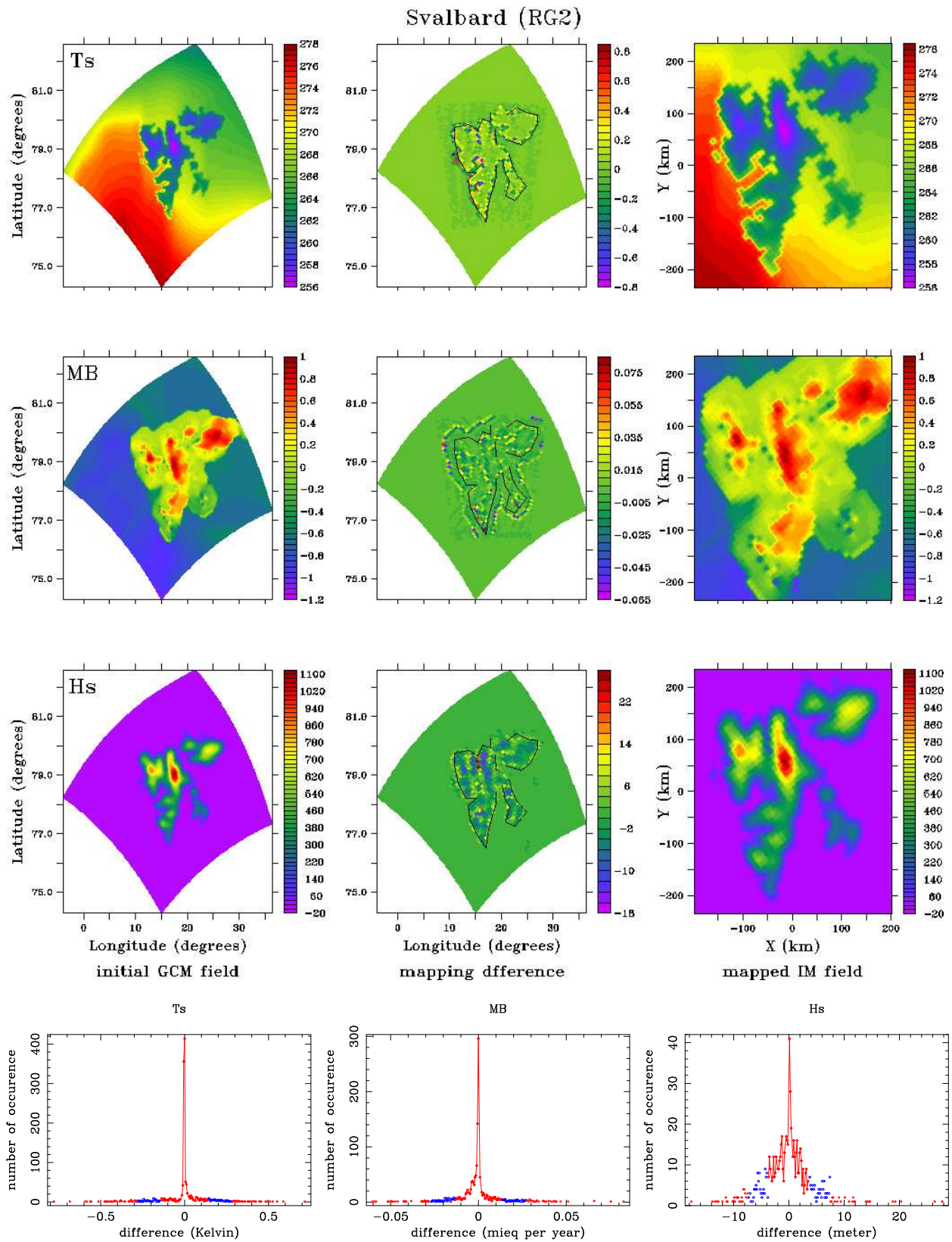


**Fig. 11.** This figure concerns Svalbard (data set RG2), see further the caption of Fig. 7.

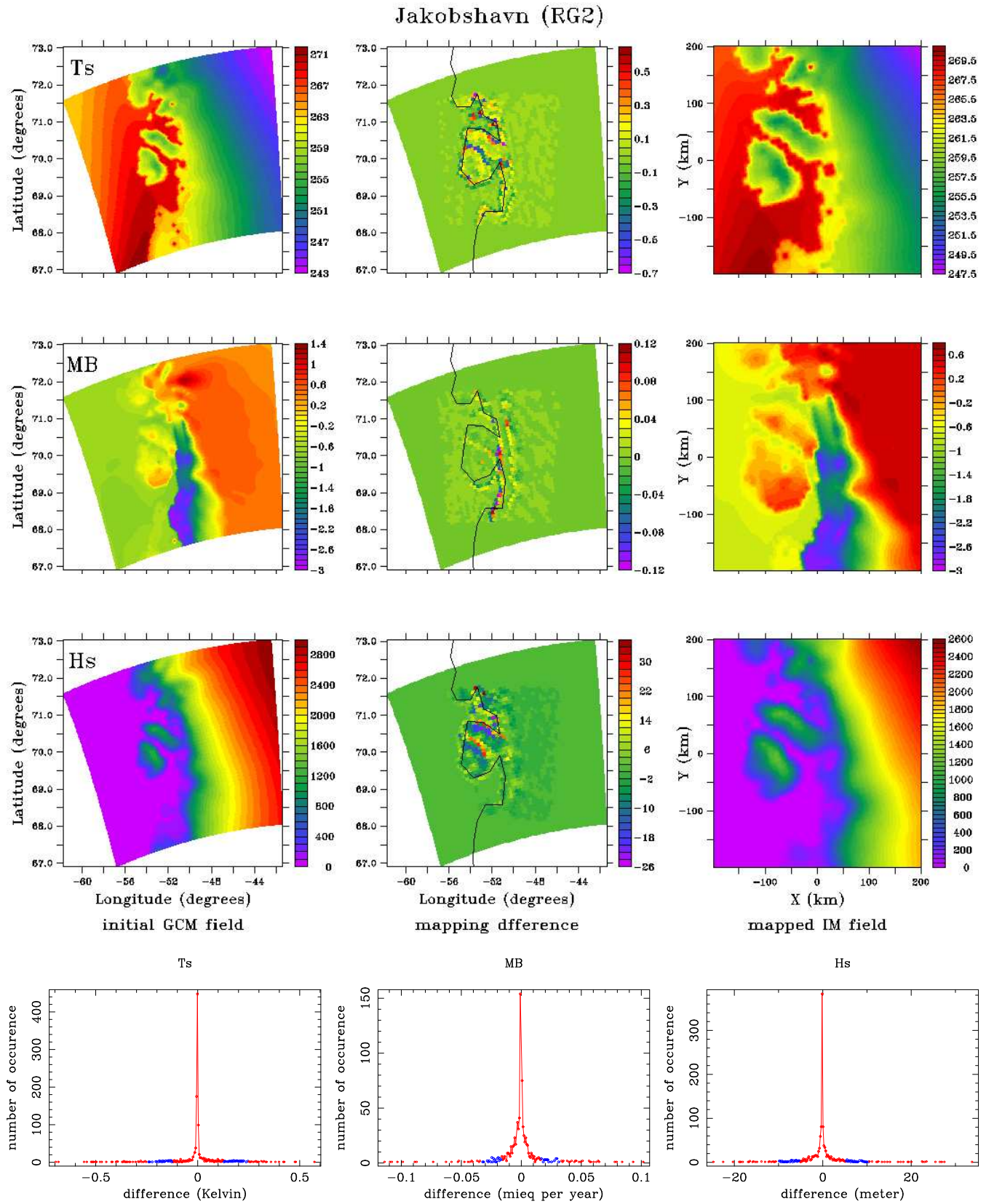


**Fig. 12.** This figure concerns Jakobshavn (data set RG2), see further the caption of Fig. 7.

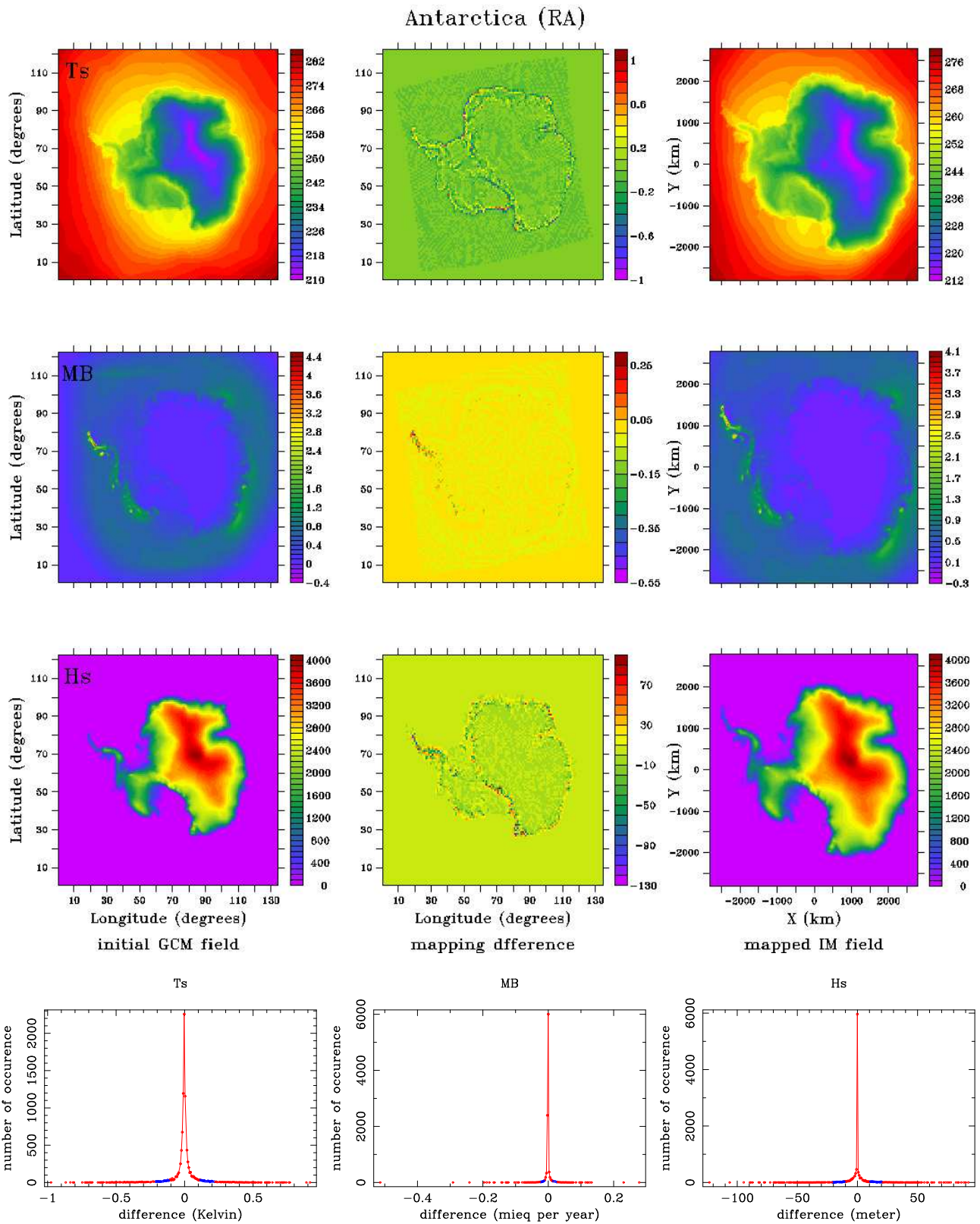


**Fig. 13.** This figure concerns Antarctica (data set RA), see further the caption of Fig. 7.



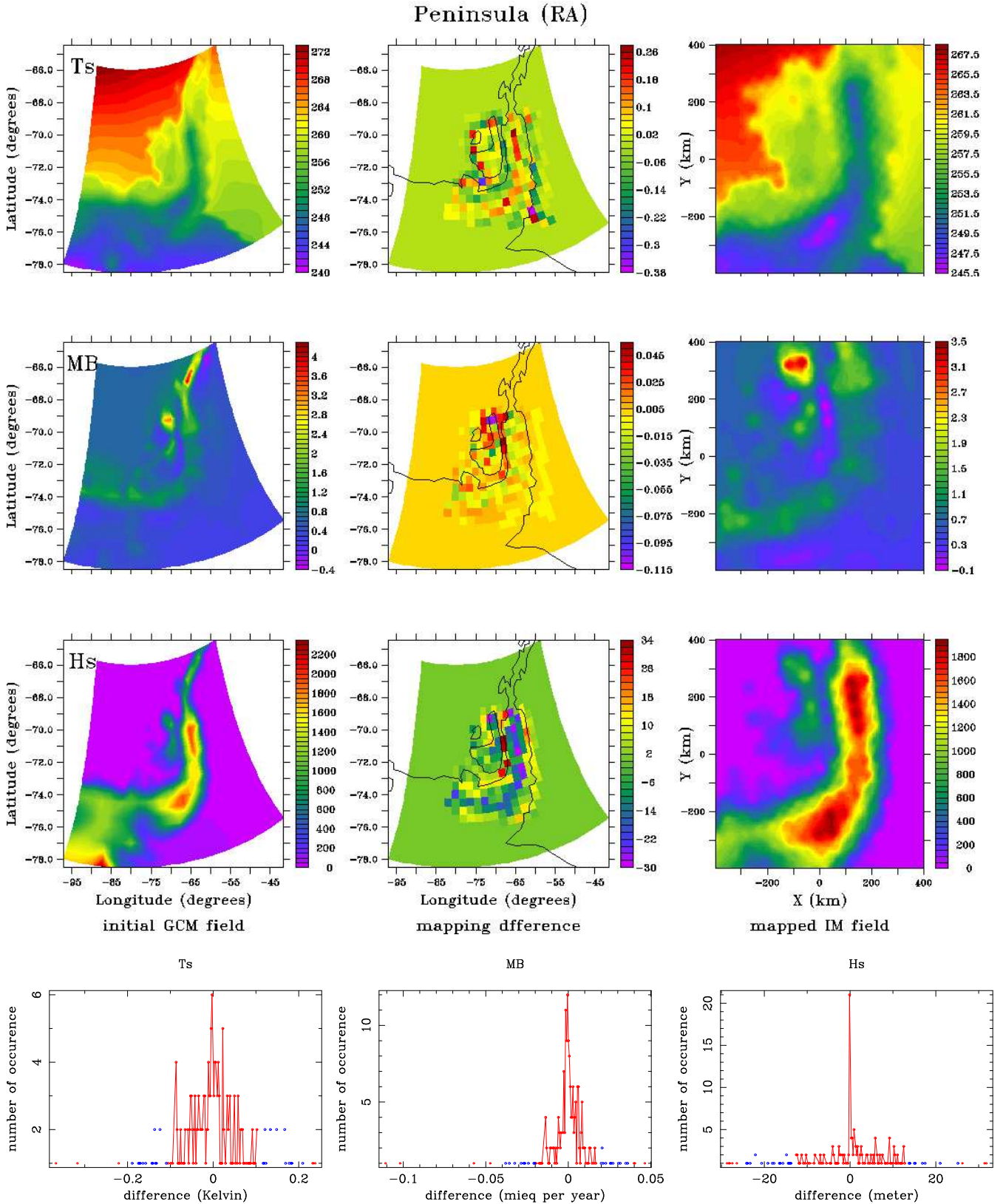


**Fig. 14.** This figure concerns Ross (data set RA), see further the caption of Fig. 7.

**Table 1.** Overview of the mapping experiments. The first column numbers the various mapping experiments for several areas and data sets. The IM grid sizes  $N_x$ ,  $N_y$ , the grid spacing  $\Delta_x=\Delta_y$  (in km), the intersection angle  $\alpha$ , and the coordinates of the middle point of interest  $M(\lambda_M, \phi_M)$  (in  $^\circ$ ) are listed. The data sets are specified in Table 2. All  $\alpha$  are as given by Eq. (2.2) except for Antarctica where a little smaller  $\alpha$  of  $19^\circ$  is used. The search radius  $R_s$  is shown for those experiments which use the radius method for the IM-GCM mapping. If  $R_s$  is absent the quadrant method is used, like for all GCM-IM mappings. And  $N$  is the amount of points which are involved in the mapping.

no	area	data set	$N_x$	$N_y$	$\Delta_x$ (km)	$\alpha$ ( $^\circ$ )	$\lambda_M$ ( $^\circ$ )	$\phi_M$ ( $^\circ$ )	$R_s$ (km)	$N$
1	Antarctica	A	281	281	20	19.0	0.0	-90.0	125.0	1268
2	Greenland	A	76	141	20	7.5	320.0	72.0	125.0	160
3	Himalaya	A	200	200	20	14.5	90.0	32.0	125.0	195
4	Greenland	RG2	153	283	10	7.5	320.0	72.0		34880
5	Ellesmere	RG2	211	281	3	2.6	278.2	79.8	4.4	4328
6	Svalbard	RG2	200	235	2	1.6	18.2	78.5	4.4	1529
7	Iceland	RG2	271	200	2	1.7	341.2	65.0	4.4	1736
8	Jakobshavn	RG2	200	200	2	1.4	308.7	70.0	4.4	1268
9	Helheim	RG2	200	200	2	1.4	323.9	67.1	4.4	1268
10	Humboldt	RG2	200	200	2	1.4	298.0	80.0	4.4	1284
11	Storstrømmen	RG2	200	200	2	1.4	336.3	76.7	4.4	1272
12	Antarctica	RA	281	281	20	19.0	0.0	-90.0		10367
13	Amery	RA	200	200	4	2.9	67.9	-73.1	22.0	206
14	Peninsula	RA	200	200	4	2.9	291.5	-72.2	22.0	204

**Table 2.** This table lists the GCM model with which each data set is created, and the area and epoch of that run. The references describe these model runs.

data set	model	area	epoch	reference
A	CCSM3	global	Dec–Feb averaged	Collins et al. (2005)
RG2	RACMO	Greenland	1990–2007 averaged	Ettema et al. (2009)
RA	RACMO	Antarctica	1980–2004 averaged	Van de Berg et al. (2006)

the AMD divided by the field range, might be more appropriate to judge the quality of the mapping. The drawback of the RRD is its dependence on the incidental field extremes. However, the fact that the RRD is for all experiments below 0.5% confirms the accuracy of the OBLIMAP mapping.

The largest deviations in experiment 4 concern the areas Ellesmere, Jakobshavn, Helheim, and Storstrømmen, containing the largest gradients with irregular patterns. These areas are locally mapped in experiments 5, 8, 9, and 11. For instance, the results of experiments 5 and 8 for Ellesmere and Jakobshavn in Figs. 10 and 12 show a detailed mapping. Note that experiment 10 for Humboldt with exactly the same mapping conditions as experiment 8 for Jakobshavn (see Table 1), reveals about two times smaller deviations because of the less complex gradients in the Humboldt fields (see Table 1).

The local experiments show smaller AMD's and smaller  $2\sigma$  intervals. This has to do with the large gradients and the smaller IM grid resolution in combination with the radius method, which is used for the IM-GCM mapping in those cases. In the local experiments the contributing points within

$R_s$  are originating predominantly from the same GCM grid points. Whereas in experiment 4 the quadrant method uses the values of the neighbour GCM points, causing larger deviations due to the large gradients.

Mapping large areas like the entire Northern Hemisphere, any other oblique Hemisphere, or even areas larger than this is possible. Select such a part of the globe by specifying an angle  $\gamma$  being equal to the angle  $ICM'$  (see Fig. 2). For a given  $\gamma$ , an optimal  $\alpha$  and a matching  $N_x\Delta x$  extent for a squared IM grid can be obtained with:

$$\alpha = 2\arctan\left(\sqrt{\frac{1}{2\pi}}\tan(\gamma)\right) \quad (4.1)$$

$$N_x\Delta x = R[1 + \cos(\alpha)]\tan(\gamma) \quad (4.2)$$

for  $0^\circ \leq \gamma \leq 90^\circ$ . With  $\gamma=45^\circ$  half the globe is mapped, yielding  $\alpha=43.5^\circ$ , and with e.g.  $N_x=200$  we have  $\Delta x=58$  km. Results of mapping the Northern Hemisphere with data set A are in line with those in Table 3, however for such extended cases the local scaling differences become rather large and the large “easy” oceanic areas suppress the average deviations.

**Table 3.** The table presents for each mapping experiment the field range and field average for comparison with the average mapped deviation (AMD) and its standard deviation ( $\sigma$ ). The AMD is the mean absolute error (MAE) of the deviations of the to and fro mapped GCM field, and is used to quantify the quality of the mapping. About 95% of the mapped field deviations (all inside the range of 94–99%) lays within the  $2\sigma$  interval. The range relative deviation RRD is the AMD divided by the field range, in percent.

no	area	data set	field range		field average	AMD	$2\sigma$	RRD (%)
<i>T<sub>s</sub></i> (Kelvin)								
1	Antarctica	A	240.2	277.6	264.6	0.04	0.18	0.11
2	Greenland	A	238.8	280.0	253.0	0.15	0.50	0.37
3	Himalaya	A	251.5	301.5	274.9	0.06	0.20	0.12
4	Greenland	RG2	240.4	282.5	260.2	0.12	0.70	0.27
5	Ellesmere	RG2	242.8	263.0	254.3	0.06	0.24	0.30
6	Svalbard	RG2	256.0	276.0	267.2	0.06	0.28	0.32
7	Iceland	RG2	265.2	281.8	276.0	0.03	0.15	0.20
8	Jakobshavn	RG2	248.5	270.8	261.6	0.05	0.25	0.23
9	Helheim	RG2	246.1	277.5	260.6	0.03	0.17	0.10
10	Humboldt	RG2	244.0	259.1	251.3	0.03	0.14	0.20
11	Storstrømmen	RG2	243.5	263.9	253.8	0.03	0.12	0.13
12	Antarctica	RA	212.0	278.5	253.3	0.05	0.22	0.07
13	Amery	RA	225.1	254.9	238.7	0.03	0.14	0.11
14	Peninsula	RA	245.8	267.8	257.3	0.06	0.22	0.28
<i>MB</i> (mieq per year)								
1	Antarctica	A	0.00	0.61	0.19	0.001	0.005	0.20
2	Greenland	A	0.12	1.17	0.40	0.003	0.014	0.33
3	Himalaya	A	0.00	1.02	0.20	0.002	0.010	0.24
4	Greenland	RG2	-3.18	4.22	-0.10	0.018	0.114	0.25
5	Ellesmere	RG2	-1.52	1.18	-0.42	0.006	0.026	0.23
6	Svalbard	RG2	-1.15	0.99	-0.17	0.006	0.027	0.30
7	Iceland	RG2	-2.46	2.07	-0.08	0.010	0.044	0.22
8	Jakobshavn	RG2	-2.91	0.71	-0.43	0.006	0.033	0.18
9	Helheim	RG2	-1.08	3.69	0.90	0.006	0.029	0.13
10	Humboldt	RG2	-1.35	0.54	-0.33	0.004	0.016	0.19
11	Storstrømmen	RG2	-1.73	0.37	-0.27	0.003	0.013	0.12
12	Antarctica	RA	-0.35	4.36	0.44	0.003	0.026	0.07
13	Amery	RA	-0.04	0.42	0.09	0.001	0.005	0.22
14	Peninsula	RA	-0.08	3.33	0.67	0.010	0.040	0.29
<i>H<sub>s</sub></i> (meter)								
1	Antarctica	A	-111	3629	871	3.1	10.9	0.08
2	Greenland	A	-65	2397	902	5.2	20.1	0.21
3	Himalaya	A	-21	5034	1502	7.7	27.6	0.15
4	Greenland	RG2	-12	3227	922	6.8	38.1	0.21
5	Ellesmere	RG2	-10	1777	305	2.8	10.9	0.16
6	Svalbard	RG2	-10	1111	116	1.7	7.4	0.15
7	Iceland	RG2	-24	1672	241	1.8	7.3	0.11
8	Jakobshavn	RG2	0	2529	788	2.2	10.4	0.09
9	Helheim	RG2	0	3088	1354	1.8	7.9	0.06
10	Humboldt	RG2	0	2220	887	1.6	6.4	0.07
11	Storstrømmen	RG2	-10	2626	1035	1.3	5.6	0.05
12	Antarctica	RA	0	4056	858	3.5	20.9	0.09
13	Amery	RA	31	3164	1880	3.2	12.1	0.10
14	Peninsula	RA	0	1930	497	7.4	25.9	0.38

**Table 4.** The table presents for each mapping experiment the difference between the area-integrated mass balance at the GCM and the IM grid:  $\Delta MB$  in mieq per year. These area-integrated differences are divided by the total mapped area, to overcome a bias due to small differences in surface size at the grid edges. With  $\delta MB$  we denote the range relative  $\Delta MB$ , which equals the  $\Delta MB$  divided by the range of  $MB$  in percent.

no	area	data set	$\Delta MB$ (mieq y <sup>-1</sup> )	$\delta MB$ (%)
1	Antarctica	A	0.003	0.45
2	Greenland	A	0.002	0.18
3	Himalaya	A	0.006	0.63
4	Greenland	RG2	0.005	0.07
5	Ellesmere	RG2	0.004	0.14
6	Svalbard	RG2	0.006	0.26
7	Iceland	RG2	0.005	0.11
8	Jakobshavn	RG2	0.010	0.27
9	Helheim	RG2	0.009	0.19
10	Humboldt	RG2	0.002	0.12
11	Storstrømmen	RG2	0.001	0.03
12	Antarctica	RA	0.004	0.09
13	Amery	RA	0.001	0.28
14	Peninsula	RA	0.004	0.10

Finally, in Table 4 we present the differences of the area-integrated mass balance per surface unit between the GCM grid and the IM grid,  $\Delta MB$  (in mieq y<sup>-1</sup>), and  $\delta MB$  (in %) which is equal to the range relative  $\Delta MB$ . Table 4 shows for our experiments nearly conserved mapping of the mass balance with  $\Delta MB \leq 0.01$  mieq y<sup>-1</sup> which is equivalent with a  $\delta MB$  typically about 0.2%.

## 5 Discussion

The oblique projection formula's are capable of performing a projection of a field defined on a grid which is based on geographical coordinates around any point at the Earth's surface with an optimal centered projection for this location. Both, Snyders and our oblique stereographic projection, yield the same results for our applications, in case we adopt  $\alpha$  into the Snyder projection instead of  $k_0$ . Working with  $\alpha$  is more intuitive, and an  $\alpha$  for an optimal projection is estimated by OBLIMAP in advance, so a least squared method (see Snyder, 1987, p. 157) can be avoided. Though, an optimal  $\alpha$  can be different from Eq. (2.2), in case the area of interest differs significantly from the total grid area. For example, one needs a relatively large grid for Antarctica to include the Peninsula branch. In that case one can choose  $\alpha$  a little bit smaller, fitting better to a one to one projection for the average continent. For example, Eq. (2.2) yields  $\alpha=20.6^\circ$  in experiments 1 and 12 for Antarctica, but we used  $19^\circ$ .

However, our equations follow a direct oblique approach which is well documented, are unique for all situations, guarantee a continuous collection of well defined Cartesian orientated projection planes over the globe, use the intuitive angle  $\alpha$  to define an optimal projection plane, and compared to Snyder (1987) our inverse projection is two times faster in computation avoiding the use of both arcsin and arccos which are vertical-asymptotic functions. Furthermore, our direct oblique methodology might be of interest in future applications of high accuracy: to derive an oblique stereographic projection and its inverse in case the Earth's surface is represented by a geoid, or by a function which is even closer to the Earth's topography. In that case  $S$  should be replaced by that function, but  $T$  remains a sphere through  $M'$ .

Repeating our applications with the Lambert azimuthal equal-area projection, reveals very similar results for both projection methods. These results are in agreement with the quotes of Snyder (1987, p. 3 and 5): “*It cannot be said that there is one “best” projection for mapping. It is even risky to claim that one has found the “best” projection for a given application*” and for areas as large as the USA: “*a trained eye cannot often distinguish whether the map is equal-area or conformal*”. For small areas the distortions are that small that an equal-area method is convenient because of its surface conservation.

For those cases that a GCM data set is provided on a grid which coincides with an ellipsoid instead of a sphere, OBLIMAP contains the equivalent oblique stereographic and the oblique Lambert azimuthal equal-area projection and their inverse for the ellipsoid (see Snyder, 1987, p. 160 and 187, respectively), with the frequently used World Geodetic System 1984 (WGS84) ellipsoid as the default. As noted by Snyder (1987) these ellipsoidal projections are not strictly perspective. The mapping accuracy with the ellipsoidal projections are in agreement with those for the sphere as expected, because the accuracy depends mainly on the interpolation.

In case the grid is irregular, in practice this concerns the GCM grid, OBLIMAP contains the option to read the 2-D fields with the longitude and latitude coordinates of the grid points. This allows the projection of fields which are defined on a grid with an arbitrary distribution, because of the combination with the quadrant and the radius interpolation method which search and weigh by distance only. The latter makes the method also robust for data gaps.

Depending on the ratio of the IM and GCM resolution and on the mapping direction, the quadrant or the radius interpolation method can be used. In case both grid resolutions are of similar size or in case the target grid is finer, the quadrant method is evidently the best option. Otherwise, in case the target grid is about four or more times coarser the radius method is most suited representing more than the centered points only. Actually, in our mapping experiments the quadrant method generates about ten times lower AMD's for those latter cases, but that is because of our experimental set up in

which we start with the coarse grid. So, we used the radius method representing a realistic and fair test of the OBLIMAP performance for those cases.

Of course the OBLIMAP performance is sensitive to data gaps, to a large difference in resolution between the IM and the GCM, and to steep gradients in combination with irregular field patterns, factors controlling any interpolation. However, OBLIMAP treats them correctly, and also the limited extent of the IM grid is treated properly, which is reflected by the results revealing no artifacts.

The OBLIMAP fortran90 code is easy to implement because it is compact and modular. Simultaneous and fast mapping of fields is possible after a first scan of both grids and by knowing the projection specifications. The scan, by far the most time consuming, comprises the projection of the grid coordinates to the target grid and the search of the nearby projected points thereafter, necessary to estimate the field value of each target grid point by interpolation. By storing the indices of the projected grid points and the distance between those points and the target grid points, a subsequent mapping consumes far less time.

The simultaneous 2-D mapping property of OBLIMAP allows mapping of 3-D fields layer by layer. Note that each layer will be treated equally with respect to the projection, i.e. no vertical adjustments are applied for the difference in  $R$ . Actually, any field is mapped as a 2-D level field, i.e. no volume conserving corrections are applied for a field like ice thickness.

Down scaling of the forcing fields after mapping will be required to match the ice topography. This part of the IM-GCM coupling is beyond the scope of the work presented here. However, because the topographic data from Bamber et al. (2001) are used for the RACMO run of Greenland, a present day equilibrium run of the Greenland ice sheet is directly possible with the mapped RACMO  $T_s$  and  $MB$  because it matches with an equally (re)mapped Bamber et al. (2001) topography.

## 6 Conclusions

This work accompanies the OBLIMAP mapping routines which are available from the GMD site (see supplementary material <http://www.geosci-model-dev.net/3/13/2010/gmd-3-13-2010-supplement.zip>). The core of these routines are the oblique and the inverse oblique stereographic and Lambert azimuthal equal-area projections for both the sphere and the WGS84 ellipsoid. Besides these optimal centered projections, the routines deal with all kinds of IM-GCM resolution ratios with respect to the interpolation on to these grids, with data gaps, with limited grid extents, with adjustable unit conversions, with merging the local IM results with the GCM data, and they incorporate a fast mapping option once a scan of the contributing projected points around each target grid point is performed.

The scan needs the grid extents. The GCM grid extents are deduced from the initial GCM grid, whereas the IM grid extents are specified by  $N_x$ ,  $N_y$ ,  $\Delta x$ ,  $\Delta y$ . An optimal intersection angle  $\alpha$  depends on the IM extents, and has to be specified. The same holds for the coordinates  $\lambda_M$  and  $\phi_M$  defining to the central point of the projection. The final scan option concerns the choice between the quadrant and the radius interpolation method for each mapping direction. In case of the radius method the search radius  $R_s$  has to be specified as well.

With three different data sets of various resolutions and based on two different GCM's (CCSM and RACMO), fourteen miscellaneous mapping experiments show accurate results for several locations. The average of the surface temperature deviations is 0.1 K or less and the  $2\sigma$  intervals are between 0.1 and 0.7 K, for all these experiments (see Table 3). The results of the surface mass balance and the surface height are more complex to interpret because relatively small deviations of large values are mixed with those of small values, however their average deviation compared to their field range deviates less than 0.4%. Considering the difference in field patterns the range relative deviations are comparable for all three quantities. With range relative mass balance deviations of a few tenth percent (see Table 4) various experiments showed nearly conserved GCM-IM mapping. To put these results in perspective, the uncertainty of the CCSM surface temperature has to be assumed to be about a few degrees (Collins et al., 2005), for RACMO-Greenland 2 K (J. Ettema, personal communication, 2009), and for RACMO-Antarctica 2–4 K (Van de Berg et al., 2007).

## Appendix A

### Derivation of the oblique stereographic projection: from GCM to IM

Each GCM point  $P$  on  $S$  is projected along  $\overrightarrow{CP}$  to  $P'$  in  $S'$ , whereupon its relative position with respect to the IM coordinates  $x_{IM}$  and  $y_{IM}$  are determined, see Fig. 2. The approach will be:

- Specifying  $\alpha$ , which defines the exact oblique stereographic projection.
- Specifying  $\lambda_M$  and  $\phi_M$  the coordinates of the middle point of interest  $M$ , with which the projection axis for any point  $P$  is known.
- Express  $M$  and  $M'$  in 3-D rectangular coordinates.
- Find a parameterized 3-D vector expression for the projection axis  $\overrightarrow{CP}$ .
- Find the 3-D rectangular coordinates of  $P'$ , which is the point of intersection of  $\overrightarrow{CP}$  and  $S'$ .

- Find the coordinates of  $P'$  relative to the IM coordinate system.

The rectangular coordinates in  $\mathbb{R}^3$  of a point  $M$  in the middle of an area of interest on  $S$  with a radius  $R$ , can be expressed in the spherical coordinates of  $M$  ( $\lambda, \phi, r$ )= $(\lambda_M, \phi_M, R)$  with use of Eq. (C2)

$$\begin{aligned} M(x^{3-D}, y^{3-D}, z^{3-D}) &= \overrightarrow{OM} = \\ R(\cos\lambda_M \cos\phi_M, \sin\lambda_M \cos\phi_M, \sin\phi_M) \end{aligned} \quad (A1)$$

Because  $M'$  is situated on  $\overrightarrow{OM}$  (see Fig. 2), we have in spherical coordinates in  $\mathbb{R}^3$

$$M' = (\lambda_{M'}, \phi_{M'}, r_{M'}) = (\lambda_M, \phi_M, R \cos\alpha) \quad (A2)$$

In rectangular coordinates in  $\mathbb{R}^3$  this becomes with use of Eq. (C2)

$$\begin{aligned} M'(x^{3-D}, y^{3-D}, z^{3-D}) &= \overrightarrow{OM'} = \\ R \cos\alpha (\cos\lambda_M \cos\phi_M, \sin\lambda_M \cos\phi_M, \sin\phi_M) \end{aligned} \quad (A3)$$

In an oblique stereographic projection an arbitrary point  $P$  (not too far from  $M$ ) on the spherical surface  $S$  is projected along the line  $\overrightarrow{CP}$  to a rectangular plane  $S'$ . The projected point  $P'$  is situated at the point of intersection of the line  $\overrightarrow{CP}$  and the plane  $S'$ . By using a parameterized 3-D vector representation  $\overrightarrow{CQ}$  along the line  $\overrightarrow{CP}$  and an equation for the plane  $S'$  we can calculate the 3-D rectangular coordinates of  $P'$ . The relative position of  $P'$  to the axes  $x_{IM}$  and  $y_{IM}$  of the IM grid give the coordinates  $x_{IM_{P'}}$  and  $y_{IM_{P'}}$  of  $P'$  in the IM grid we are looking for. For the latter step we need the parameterized 3-D vector representations of the IM grid axes  $l_{x_{IM}}^{3-D}$  and  $l_{y_{IM}}^{3-D}$ .

## A1 Determine $P'$

In this section we will determine the 3-D rectangular coordinates of the projected point  $P'$ . In Sect. A1.1 a parameter representation for the vector  $\overrightarrow{CQ}$  along the line  $\overrightarrow{CP}$  is given, and in Sect. A1.2 an equation for the plane  $S'$ . In Sect. A1.3 we determine the parameter value  $t_{P'}$  belonging to the point  $P'$ , the intersection point of  $\overrightarrow{CQ}$  and  $S'$ . In the last step, in Sect. A1.4, we substitute this  $t_{P'}$  into the parameter representation of  $\overrightarrow{CQ}$  to obtain the coordinates of  $P'$ .

### A1.1 The parameter representation $\overrightarrow{CQ}$

For each arbitrary point  $P=(\lambda_P, \phi_P, R)$  on  $S$  the vector  $\overrightarrow{OP}$  in 3-D rectangular coordinates is

$$\begin{aligned} P(x^{3-D}, y^{3-D}, z^{3-D}) &= \overrightarrow{OP} \\ &= R(\cos\lambda_P \cos\phi_P, \sin\lambda_P \cos\phi_P, \sin\phi_P) \end{aligned} \quad (A4)$$

If  $Q$  is a point situated on the line  $\overrightarrow{CP}$  then the parameter representation of  $\overrightarrow{CQ}$  can be given by

$$\overrightarrow{CQ} = \overrightarrow{OC} + (\overrightarrow{OP} - \overrightarrow{OC})t \quad \text{for some } t \in \mathbb{R} \quad (A5)$$

Because  $C$  and  $M$  are anti-poles we have

$$\overrightarrow{OC} = -\overrightarrow{OM} \quad (A6)$$

this substituted in Eq. (A5) gives

$$\overrightarrow{CQ} = -\overrightarrow{OM} + (\overrightarrow{OP} + \overrightarrow{OM})t \quad (A7)$$

which becomes with Eq. (A1) and Eq. (A4)

$$\begin{aligned} \overrightarrow{CQ} &= -R(\cos\lambda_M \cos\phi_M, \sin\lambda_M \cos\phi_M, \sin\phi_M) \\ &\quad + R(\cos\lambda_P \cos\phi_P + \cos\lambda_M \cos\phi_M, \sin\lambda_P \cos\phi_P \\ &\quad + \sin\lambda_M \cos\phi_M, \sin\phi_P + \sin\phi_M)t \end{aligned}$$

So the coordinates of  $Q$  on  $\overrightarrow{CQ}=(x_Q^{3-D}, y_Q^{3-D}, z_Q^{3-D})$  expressed in  $t$  are

$$x_Q^{3-D} = R((\cos\lambda_M \cos\phi_M)(t-1) + (\cos\lambda_P \cos\phi_P)t) \quad (A8)$$

$$y_Q^{3-D} = R((\sin\lambda_M \cos\phi_M)(t-1) + (\sin\lambda_P \cos\phi_P)t) \quad (A9)$$

$$z_Q^{3-D} = R((\sin\phi_M)(t-1) + (\sin\phi_P)t) \quad (A10)$$

### A1.2 The equation of $S'$

Because  $\overrightarrow{OM}$  is perpendicular to  $S'$  we can take the components of  $M$  (see Eq. A1) as the normal vector  $N_{S'}$  for  $S'$

$$\begin{aligned} N_{S'}(x^{3-D}, y^{3-D}, z^{3-D}) \\ = (\cos\lambda_M \cos\phi_M, \sin\lambda_M \cos\phi_M, \sin\phi_M) \end{aligned} \quad (A11)$$

Using this as the normal vector in Eq. (C3), this gives an equation for  $S'$

$$S': \cos\lambda_M \cos\phi_M x^{3-D} + \sin\lambda_M \cos\phi_M y^{3-D} + \sin\phi_M z^{3-D} = k \quad (A12)$$

for some  $k \in \mathbb{R}$ . To determine  $k$  we fill in  $M'$  (see Eq. A3) because it is part of  $S'$ , to obtain the final equation for  $S'$ :

$$\begin{aligned} S': \cos\lambda_M \cos\phi_M x^{3-D} + \sin\lambda_M \cos\phi_M y^{3-D} + \sin\phi_M z^{3-D} \\ = R \cos\alpha \end{aligned} \quad (A13)$$

### A1.3 Determining the parameter $t=t_{P'}$ for $P'$

$P'$  is situated at the intersection of  $\overrightarrow{CQ}$  and  $S'$ . To obtain  $t_{P'}$  we substitute the 3-D rectangular coordinates of  $Q=P'$  given by Eqs. (A8)–(A10) for  $t=t_{P'}$  into the plane Eq. (A13) for  $S'$

$$\begin{aligned} \cos\lambda_M \cos\phi_M [R((\cos\lambda_M \cos\phi_M)(t_{P'}-1) + (\cos\lambda_P \cos\phi_P)t_{P'})] \\ + \sin\lambda_M \cos\phi_M [R((\sin\lambda_M \cos\phi_M)(t_{P'}-1) + (\sin\lambda_P \cos\phi_P)t_{P'})] \\ + \sin\phi_M [R((\sin\phi_M)(t_{P'}-1) + (\sin\phi_P)t_{P'})] \\ = R \cos\alpha \end{aligned}$$

which equals

$$(t_{P'} - 1) + [\cos\phi_M \cos\phi_P (\cos\lambda_M \cos\lambda_P + \sin\lambda_M \sin\lambda_P) + \sin\phi_M \sin\phi_P] t_{P'} = \cos\alpha$$

and with Eq. (C5) this becomes

$$(1 + \cos\phi_M \cos\phi_P \cos(\lambda_M - \lambda_P) + \sin\phi_M \sin\phi_P) t_{P'} = 1 + \cos\alpha$$

so finally we get for  $t_{P'}$

$$t_{P'} = \frac{1 + \cos\alpha}{1 + \cos\phi_M \cos\phi_P \cos(\lambda_M - \lambda_P) + \sin\phi_M \sin\phi_P} \quad (\text{A14})$$

#### A1.4 The coordinates of $P'$

Substitution of  $t=t_{P'}$  given by Eq. (A14) into Eqs. (A8)–(A10) for  $Q$ , gives the coordinates of  $P'$ . So the coordinates of  $P'$  are given by

$$x_{P'}^{3-D} = R((\cos\lambda_M \cos\phi_M)(t_{P'} - 1) + (\cos\lambda_P \cos\phi_P)t_{P'}) \quad (\text{A15})$$

$$y_{P'}^{3-D} = R((\sin\lambda_M \cos\phi_M)(t_{P'} - 1) + (\sin\lambda_P \cos\phi_P)t_{P'}) \quad (\text{A16})$$

$$z_{P'}^{3-D} = R((\sin\phi_M)(t_{P'} - 1) + (\sin\phi_P)t_{P'}) \quad (\text{A17})$$

with

$$t_{P'} = \frac{1 + \cos\alpha}{1 + \cos\phi_M \cos\phi_P \cos(\lambda_M - \lambda_P) + \sin\phi_M \sin\phi_P} \quad (\text{A18})$$

#### A2 The parameter representations of the IM grid axes

The IM grid coincides with the plane  $S'$ . The origin of the IM axes  $x_{\text{IM}}$  and  $y_{\text{IM}}$  coincides with the point  $M' = (x_{\text{IM}} = 0, y_{\text{IM}} = 0)$ . In this section we will obtain the parameter representations  $l_{x_{\text{IM}}}^{3-D}$  and  $l_{y_{\text{IM}}}^{3-D}$  for the  $x_{\text{IM}}$  and  $y_{\text{IM}}$  axes respectively, in the 3-D rectangular coordinates.

##### A2.1 The inner help sphere $T$

We introduce an extra inner help sphere  $T$  which goes through  $M'$  with  $O$  as origin. Because  $T$  goes through  $M'$  the radius of  $T$  is  $R_T = R \cos\alpha$ . The plane  $S'$  is the tangent plane in  $M'$  to this help sphere  $T$ . The tangent line to  $T$  in the positive  $\lambda$  direction at point  $M'$  in the plane  $S'$  is chosen to coincide with the positive  $x_{\text{IM}}$  axis, while the tangent line to  $T$  in the positive  $\phi$  direction at point  $M'$  in the plane  $S'$  is chosen to coincide with the positive  $y_{\text{IM}}$  axis. To calculate the 3-D parameter representations of these  $x_{\text{IM}}$  and  $y_{\text{IM}}$  axes of the IM grid we need respectively the derivatives in  $\lambda$  and  $\phi$  direction of  $T$  in  $M'$ .

The 3-D rectangular coordinates of  $T$  can with Eq. (C2) be given as

$$T(x^{3-D}, y^{3-D}, z^{3-D}) = R \cos\alpha (\cos\lambda \cos\phi, \sin\lambda \cos\phi, \sin\phi) \quad (\text{A19})$$

##### A2.2 The $\lambda$ and $\phi$ -derivatives in $M'$ on $T$

The  $\lambda$ -derivative on the spherical surface  $T$  in rectangular coordinates is

$$\begin{aligned} \partial_\lambda T(x^{3-D}, y^{3-D}, z^{3-D}) &= \partial_\lambda (R \cos\alpha (\cos\lambda \cos\phi, \sin\lambda \cos\phi, \sin\phi)) \\ &= R \cos\alpha \cos\phi (-\sin\lambda, \cos\lambda, 0) \end{aligned} \quad (\text{A20})$$

with norm

$$\left| \partial_\lambda T(x^{3-D}, y^{3-D}, z^{3-D}) \right| = R \cos\alpha |\cos\phi| \quad (\text{A21})$$

The normalized  $\lambda$ -derivative vector in point  $M'$  is then

$$\overline{\partial_\lambda T(M')} = \frac{\cos\phi_M}{|\cos\phi_M|} (-\sin\lambda_M, \cos\lambda_M, 0) \quad (\text{A22})$$

For the range  $-90^\circ < \phi_M < 90^\circ$  we have that

$$\frac{\cos\phi_M}{|\cos\phi_M|} = 1 \quad (\text{A23})$$

Except for the north and the south pole, which should be treated separately anyhow because  $\lambda$  is not unambiguous at the poles, Eq. (A22) becomes

$$\overline{\partial_\lambda T(M')} = (-\sin\lambda_M, \cos\lambda_M, 0) \quad \text{for } -90^\circ < \phi_M < 90^\circ \quad (\text{A24})$$

The  $\phi$ -derivative on the spherical surface  $T$  in rectangular coordinates is

$$\begin{aligned} \partial_\phi T(x^{3-D}, y^{3-D}, z^{3-D}) &= \partial_\phi (R \cos\alpha (\cos\lambda \cos\phi, \sin\lambda \cos\phi, \sin\phi)) \\ &= R \cos\alpha (-\cos\lambda \sin\phi, -\sin\lambda \sin\phi, \cos\phi) \end{aligned} \quad (\text{A25})$$

with norm

$$\left| \partial_\phi T(x^{3-D}, y^{3-D}, z^{3-D}) \right| = R \cos\alpha \quad (\text{A26})$$

The normalized  $\phi$ -derivative vector in point  $M'$  is then

$$\overline{\partial_\phi T(M')} = (-\cos\lambda_M \sin\phi_M, -\sin\lambda_M \sin\phi_M, \cos\phi_M) \quad (\text{A27})$$

##### A2.3 The parameter representations of $l_{x_{\text{IM}}}^{3-D}$ and $l_{y_{\text{IM}}}^{3-D}$

The parameter representations  $l_{x_{\text{IM}}}^{3-D}$  and  $l_{y_{\text{IM}}}^{3-D}$  describe respectively the  $x_{\text{IM}}$  and the  $y_{\text{IM}}$  axes in 3-D rectangular coordinates with parameters  $u$  and  $v$ , respectively:

$$l_{x_{\text{IM}}}^{3-D} = \overrightarrow{OM'} + d_{l_{x_{\text{IM}}}}^{3-D} u \quad \text{for some } u \in \mathbb{R} \quad (\text{A28})$$

$$l_{y_{\text{IM}}}^{3-D} = \overrightarrow{OM'} + d_{l_{y_{\text{IM}}}}^{3-D} v \quad \text{for some } v \in \mathbb{R} \quad (\text{A29})$$

Here are  $d_{l_{x_{\text{IM}}}}^{3-D}$  and  $d_{l_{y_{\text{IM}}}}^{3-D}$  the normalized  $x_{\text{IM}}$  and  $y_{\text{IM}}$ -directions respectively. Actually  $u$  and  $v$  are the  $x_{\text{IM}}$  and  $y_{\text{IM}}$

coordinates of some point in  $S'$ , because their values are the values along the axes and relative to the origin  $M'$  of the IM grid.

The plane  $S'$  is the tangent plane in  $M'$  to  $T$ . The tangent line to  $T$  in the positive  $\lambda$  direction at point  $M'$  in the plane  $S'$  is chosen to coincide with the positive  $x_{\text{IM}}$  axis, while the tangent line to  $T$  in the positive  $\phi$  direction at point  $M'$  in the plane  $S'$  is chosen to coincide with the positive  $y_{\text{IM}}$  axis.

Therefore the  $\lambda$ -derivative on  $T$  in  $M'$  gives the direction of the  $x_{\text{IM}}$ -axis and the  $\phi$ -derivative on  $T$  in  $M'$  gives the direction of the  $y_{\text{IM}}$ -axis. So the normalized  $\lambda$ -derivative vector in  $M'$  equals the normalized  $x_{\text{IM}}$  direction vector and the normalized  $\phi$ -derivative vector in  $M'$  equals the normalized  $y_{\text{IM}}$  direction vector

$$d_{l_{x_{\text{IM}}}}^{3-\text{D}} = \overline{\partial_{\lambda} T(M')} \quad (\text{A30})$$

$$d_{l_{y_{\text{IM}}}}^{3-\text{D}} = \overline{\partial_{\phi} T(M')} \quad (\text{A31})$$

In this paragraph, we only consider the oblique cases. Because the  $\lambda$ -direction is undetermined for the polar cases with  $\phi_M = -90^\circ$  and  $\phi_M = 90^\circ$ , they will be handled in the next paragraph. Then, substituting Eqs. (A24) and Eq. (A27) respectively in Eqs. (A30)–(A31) we get

$$\overrightarrow{d_{l_{x_{\text{IM}}}}^{3-\text{D}}} = (-\sin\lambda_M, \cos\lambda_M, 0) \quad (\text{A32})$$

$$\overrightarrow{d_{l_{y_{\text{IM}}}}^{3-\text{D}}} = (-\cos\lambda_M \sin\phi_M, -\sin\lambda_M \sin\phi_M, \cos\phi_M) \quad (\text{A33})$$

Using Eq. (A3) and respectively Eqs. (A32)–(A33) in Eqs. (A28)–(A29) we obtain

$$l_{x_{\text{IM}}}^{3-\text{D}} = R \cos\alpha (\cos\lambda_M \cos\phi_M, \sin\lambda_M \cos\phi_M, \sin\phi_M) + (-\sin\lambda_M, \cos\lambda_M, 0)u \quad (\text{A34})$$

$$l_{y_{\text{IM}}}^{3-\text{D}} = R \cos\alpha (\cos\lambda_M \cos\phi_M, \sin\lambda_M \cos\phi_M, \sin\phi_M) + (-\cos\lambda_M \sin\phi_M, -\sin\lambda_M \sin\phi_M, \cos\phi_M)v \quad (\text{A35})$$

#### A2.4 The $l_{x_{\text{IM}}}^{3-\text{D}}$ and $l_{y_{\text{IM}}}^{3-\text{D}}$ including the SP and the NP

In case of a polar stereographic projection the chosen  $M$  coincides with the SP or the NP with  $\phi_{M=\text{SP}} = -90^\circ$  or  $\phi_{M=\text{NP}} = 90^\circ$  respectively. In those cases we need perpendicular cartesian IM coordinates as well, but the lambda direction is undefined, so we can not use Eq. (A24). Therefore, in the polar cases, we take the limit of the  $\phi$ -derivative vector in point  $M'$  (study e.g. Fig. 2) and take that direction as the  $\overrightarrow{d_{l_{x_{\text{IM}}}}^{3-\text{D}}}$ . The  $\overrightarrow{d_{l_{x_{\text{IM}}}}^{3-\text{D}}}$  is constructed perpendicular to this  $\overrightarrow{d_{l_{y_{\text{IM}}}}^{3-\text{D}}}$  such that they form a cartesian coordinate system pointing outward. The parameter representation for the south pole ( $\phi_M = -90^\circ$ ) becomes

$$l_{x_{\text{IM}}}^{3-\text{D}} = (0, 0, -R \cos\alpha) + (0, 1, 0)u \quad (\text{A36})$$

$$l_{y_{\text{IM}}}^{3-\text{D}} = (0, 0, -R \cos\alpha) + (1, 0, 0)v \quad (\text{A37})$$

And the parameter representation for the north pole ( $\phi_M = 90^\circ$ ) becomes

$$l_{x_{\text{IM}}}^{3-\text{D}} = (0, 0, R \cos\alpha) + (0, 1, 0)u \quad (\text{A38})$$

$$l_{y_{\text{IM}}}^{3-\text{D}} = (0, 0, R \cos\alpha) + (-1, 0, 0)v \quad (\text{A39})$$

Taking the undetermined  $\lambda_M$  equal to zero in Eqs. (A34)–(A35) gives exactly the required parameter representations for both polar cases as in Eqs. (A36)–(A39). So, conveniently, under the condition

$$\lambda_M = 0 \quad \text{for} \quad \phi_M = -90 \quad \& \quad \phi_M = 90 \quad (\text{A40})$$

for all projection cases the same parameter representations

$$l_{x_{\text{IM}}}^{3-\text{D}} = R \cos\alpha (\cos\lambda_M \cos\phi_M, \sin\lambda_M \cos\phi_M, \sin\phi_M) + (-\sin\lambda_M, \cos\lambda_M, 0)u \quad (\text{A41})$$

$$l_{y_{\text{IM}}}^{3-\text{D}} = R \cos\alpha (\cos\lambda_M \cos\phi_M, \sin\lambda_M \cos\phi_M, \sin\phi_M) + (-\cos\lambda_M \sin\phi_M, -\sin\lambda_M \sin\phi_M, \cos\phi_M)v \quad (\text{A42})$$

can be used. Writing the components separately for the parameter representation  $l_{x_{\text{IM}}}^{3-\text{D}}$  which describes the  $x_{\text{IM}}$  axis in the 3-D rectangular coordinate system we have (see Eq. A41)

$$l_{x_{\text{IM}}}^{3-\text{D}} : \begin{cases} x^{3-\text{D}} = R \cos\alpha \cos\lambda_M \cos\phi_M - (\sin\lambda_M)u \\ y^{3-\text{D}} = R \cos\alpha \sin\lambda_M \cos\phi_M + (\cos\lambda_M)u \\ z^{3-\text{D}} = R \cos\alpha \quad \sin\phi_M \end{cases} \quad (\text{A43})$$

Writing the components separate for the parameter representation  $l_{y_{\text{IM}}}^{3-\text{D}}$  which describes the  $y_{\text{IM}}$  axis in the 3-D rectangular coordinate system we have (see Eq. A42)

$$l_{y_{\text{IM}}}^{3-\text{D}} : \begin{cases} x^{3-\text{D}} = R \cos\alpha \cos\lambda_M \cos\phi_M - (\cos\lambda_M \sin\phi_M)v \\ y^{3-\text{D}} = R \cos\alpha \sin\lambda_M \cos\phi_M - (\sin\lambda_M \sin\phi_M)v \\ z^{3-\text{D}} = R \cos\alpha \quad \sin\phi_M + (\cos\phi_M)v \end{cases} \quad (\text{A44})$$

Both parameter equations Eqs. (A43)–(A44) hold for any specified coordinate  $M$ .

#### A3 The coordinates $x_{\text{IM}P'}$ and $y_{\text{IM}P'}$

The relative position of  $P'$  to the  $l_{x_{\text{IM}}}^{3-\text{D}}$  and  $l_{y_{\text{IM}}}^{3-\text{D}}$  axes of the IM grid give the coordinates  $x_{\text{IM}P'}$  and  $y_{\text{IM}P'}$  of  $P'$  in the IM grid.  $P'$ ,  $l_{x_{\text{IM}}}^{3-\text{D}}$  and  $l_{y_{\text{IM}}}^{3-\text{D}}$  are all situated in the plane  $S'$ . We create a plane  $W_1$  (see Fig. A1) which is perpendicular to the line  $l_{x_{\text{IM}}}^{3-\text{D}}$  and through  $P'$ , the point of intersection of  $W_1$  with  $l_{y_{\text{IM}}}^{3-\text{D}}$  we call point  $Q_1$ . Substituting the coordinates of the parameter representation  $l_{x_{\text{IM}}}^{3-\text{D}}$  into the equation for plane  $W_1$  will give the value of  $u = u_{P'}$  which equals the  $x_{\text{IM}P'}$  coordinate. Analogue we create a plane  $W_2$  (see Fig. A2) which is perpendicular to the line  $l_{y_{\text{IM}}}^{3-\text{D}}$  and through  $P'$ , the point of



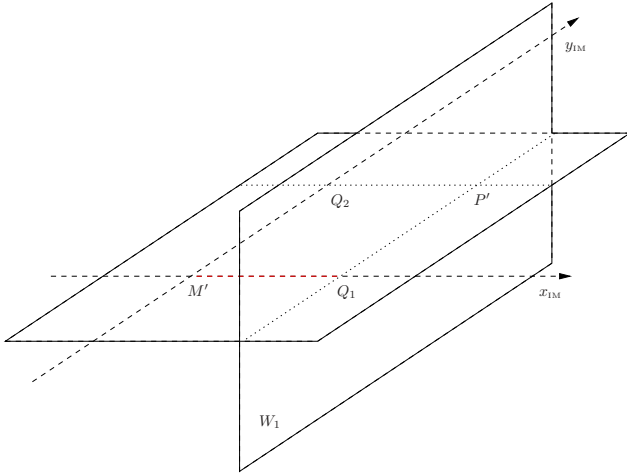


**Fig. A1.** The figure shows how plane  $W_1$  is created: perpendicular to the  $l_{xIM}^{3-D}$  axis and through  $P'$ . The red distance between  $M'$  and  $Q_1$  is  $u = u_{P'}$  which is the value of the  $x_{IM_{P'}}$  coordinate.

intersection of  $W_2$  with  $l_{yIM}^{3-D}$  we call point  $Q_2$ . Substituting the coordinates of the parameter representation  $l_{yIM}^{3-D}$  into the equation for plane  $W_2$  will give the value of  $v = v_{P'}$  which equals the  $y_{IM_{P'}}$  coordinate.

To calculate  $u_{P'}$  and  $v_{P'}$  we first have to find the equations for the planes  $W_1$  and  $W_2$ .

### A3.1 The equation for plane $W_1$

Because  $\overrightarrow{d_{l_{xIM}^{3-D}}}$  (see Eq. A32) is a normal vector to  $W_1$ , in combination with Eq. (C3), we can create an equation for the plane  $W_1$  (see Fig. A1)

$$W_1: (-\sin\lambda_M)x^{3-D} + (\cos\lambda_M)y^{3-D} = k_1 \quad (\text{A45})$$

Note that under condition (A40) this equation holds for all projection cases. To determine  $k_1$  we substitute the point  $P'$  situated in plane  $W_1$ , the coordinates of  $P'$  are given by Eqs. (A15)–(A17)

$$\begin{aligned} & -(\sin\lambda_M)R((\cos\lambda_M\cos\phi_M)(t_{P'} - 1) + (\cos\lambda_P\cos\phi_P)t_{P'}) \\ & + (\cos\lambda_M)R((\sin\lambda_M\cos\phi_M)(t_{P'} - 1) + (\sin\lambda_P\cos\phi_P)t_{P'}) = k_1 \end{aligned}$$

The left terms cancel and we get

$$k_1 = R(\cos\phi_P)(\sin\lambda_P\cos\lambda_M - \cos\lambda_P\sin\lambda_M)t_{P'}$$

and with use of Eq. (C6) we obtain

$$k_1 = R(\cos\phi_P \sin(\lambda_P - \lambda_M))t_{P'} \quad (\text{A46})$$

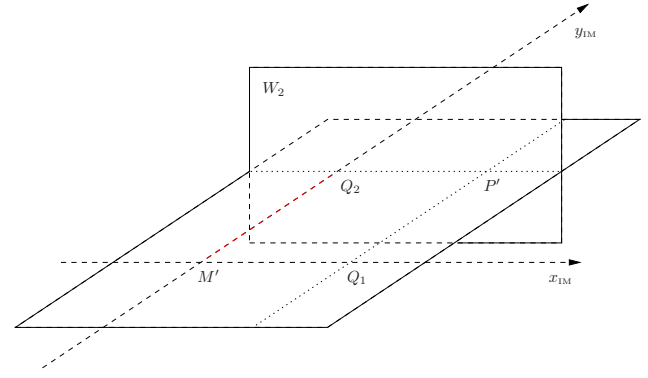


**Fig. A2.** The figure shows how plane  $W_2$  is created: perpendicular to the  $l_{xIM}^{3-D}$  axis and through  $P'$ . The red distance between  $M'$  and  $Q_2$  is  $v = v_{P'}$  which is the value of the  $y_{IM_{P'}}$  coordinate.

### A3.2 Calculation of the parameter $u = u_{P'}$

Substituting the coordinates of the parameter representation  $l_{xIM}^{3-D}$  (A43) into Eq. (A45) for plane  $W_1$ , gives the  $u = u_{P'}$  for  $Q_1$

$$\begin{aligned} & -(\sin\lambda_M)(R\cos\alpha\cos\lambda_M\cos\phi_M - (\sin\lambda_M)u_{P'}) \\ & + (\cos\lambda_M)(R\cos\alpha\sin\lambda_M\cos\phi_M + (\cos\lambda_M)u_{P'}) = k_1 \end{aligned}$$

The left terms cancel so we get

$$u_{P'} = k_1$$

filling in Eq. (A46) for  $k_1$  we get under condition (A40) for all projection cases

$$u_{P'} = R(\cos\phi_P \sin(\lambda_P - \lambda_M))t_{P'} \quad (\text{A47})$$

which is the  $x_{IM_{P'}}$  coordinate we are looking for.

### A3.3 The equation for plane $W_2$

Because  $\overrightarrow{d_{l_{yIM}^{3-D}}}$  (see Eq. A33) is a normal vector to  $W_2$ , in combination with Eq. (C3), we can create an equation for the plane  $W_2$  (see Fig. A2)

$$\begin{aligned} & (-\cos\lambda_M\sin\phi_M)x^{3-D} + \\ & (-\sin\lambda_M\sin\phi_M)y^{3-D} + (\cos\phi_M)z^{3-D} = k_2 \end{aligned} \quad (\text{A48})$$

To determine  $k_2$  we substitute the point  $P'$  situated in plane  $W_2$ , the coordinates of  $P'$  are given by Eqs. (A15)–(A17)

$$\begin{aligned} & -(\cos\lambda_M\sin\phi_M)R((\cos\lambda_M\cos\phi_M)(t_{P'} - 1) + (\cos\lambda_P\cos\phi_P)t_{P'}) \\ & -(\sin\lambda_M\sin\phi_M)R((\sin\lambda_M\cos\phi_M)(t_{P'} - 1) + (\sin\lambda_P\cos\phi_P)t_{P'}) \\ & + (\cos\phi_M)R((\sin\phi_M)(t_{P'} - 1) + (\sin\phi_P)t_{P'}) = k_2 \end{aligned}$$

The left terms cancel and we get

$$k_2 = -R[(\sin\phi_M \cos\phi_P)(\cos\lambda_M \cos\lambda_P + \sin\lambda_M \sin\lambda_P) - \cos\phi_M \sin\phi_P]t_{P'}$$

which becomes with Eq. (C5)

$$k_2 = R[\cos\phi_M \sin\phi_P - (\sin\phi_M \cos\phi_P)\cos(\lambda_M - \lambda_P)]t_{P'} \quad (\text{A49})$$

### A3.4 Calculation of the parameter $v=v_{P'}$

Substituting the coordinates of the parameter representation  $l_{y_{IM}}^{3-D}$  (A44) into Eq. (A48) for the plane  $W_2$ , gives the  $v$  for  $Q_2$

$$\begin{aligned} & -(\cos\lambda_M \sin\phi_M)(R\cos\alpha \cos\lambda_M \cos\phi_M - (\cos\lambda_M \sin\phi_M)v_{P'}) \\ & -(\sin\lambda_M \sin\phi_M)(R\cos\alpha \sin\lambda_M \cos\phi_M - (\sin\lambda_M \sin\phi_M)v_{P'}) \\ & +(\cos\phi_M)(R\cos\alpha \sin\phi_M + (\cos\phi_M)v_{P'}) = k_2 \end{aligned}$$

The left terms cancel and the right terms just add to one times  $v_{P'}$ , with Eq. (A49) for  $k_2$  resulting in

$$v_{P'} = k_2 = R[\cos\phi_M \sin\phi_P - (\sin\phi_M \cos\phi_P)\cos(\lambda_P - \lambda_M)]t_{P'} \quad (\text{A50})$$

which is the  $y_{IM_{P'}}$  coordinate we are looking for.

### A4 The final oblique stereographic projection

The longitude-latitude coordinates  $\lambda_P$  and  $\phi_P$  of an arbitrary point  $P$  on the spherical surface  $S$  are projected to a rectangular plane  $S'$  which coincides with the IM grid with origin  $M'$ . As soon as the middle point of the area of interest on  $S$  is known by specifying  $\lambda_M$  and  $\phi_M$  the coordinates  $x_{IM_{P'}}$  and  $y_{IM_{P'}}$  of the projected point  $P'$  relative to the IM grid can be calculated by

$$x_{IM_{P'}} = u_{P'} \quad (\text{A51})$$

$$y_{IM_{P'}} = v_{P'} \quad (\text{A52})$$

The final result for the oblique stereographic projection is (see Eqs. A47, A50, and A18) under the condition (see Eq. A40)

$$\lambda_M = 0^\circ \quad \text{for} \quad \phi_M = -90^\circ \quad \& \quad \phi_M = 90^\circ \quad (\text{A53})$$

we have

$$x_{IM_{P'}} = R(\cos\phi_P \sin(\lambda_P - \lambda_M))t_{P'} \quad (\text{A54})$$

$$y_{IM_{P'}} = R[\sin\phi_P \cos\phi_M - (\cos\phi_P \sin\phi_M)\cos(\lambda_P - \lambda_M)]t_{P'} \quad (\text{A55})$$

with

$$t_{P'} = \frac{1 + \cos\alpha}{1 + \cos\phi_P \cos\phi_M \cos(\lambda_P - \lambda_M) + \sin\phi_P \sin\phi_M} \quad (\text{A56})$$

## Appendix B

### Derivation of the inverse oblique stereographic projection: from IM to GCM

In the inverse oblique stereographic projection the point  $P'$  with IM coordinates  $x_{IM_{P'}}$  and  $y_{IM_{P'}}$  is known, so in this case we have to find the longitude-latitude coordinates  $\lambda_P$  and  $\phi_P$  of point  $P$ . Point  $P$  is obtained by projecting  $P'$  which is situated in plane  $S'$ , to the spherical surface  $S$  along the line  $\overrightarrow{CP'}$ . We have to calculate the 3-D rectangular coordinates of  $P$ , with which  $\lambda_P$  and  $\phi_P$  can be determined.

But first we need a parameter representation  $\overrightarrow{CQ}$  along  $\overrightarrow{CP'}$  to determine the parameter  $t=t_P$  for its point of intersection with  $S$ . To prepare the construction of  $\overrightarrow{CQ}$ , we first express  $\overrightarrow{OP'}$  in the given IM coordinates  $x_{IM_{P'}}$  and  $y_{IM_{P'}}$ . And for  $S$  we need an equation of the spherical surface.

### B1 Determining $P$

Projecting a point  $P'$ , which is situated in plane  $S'$ , along the line  $\overrightarrow{CP'}$  on the spherical surface  $S$  gives the projected point  $P$ . We have to calculate the 3-D rectangular coordinates of  $P$ . First we express  $\overrightarrow{OP'}$  in the given IM coordinates  $x_{IM_{P'}}$  and  $y_{IM_{P'}}$ . Then we use  $\overrightarrow{OM}$  and  $\overrightarrow{OP'}$  to create the parameter representation  $\overrightarrow{CQ}$ . The parameter  $t$  at the point of intersection of  $\overrightarrow{CQ}$  and  $S$  is obtained by substituting the coordinates of  $\overrightarrow{CQ}$  with  $t=t_P$  into the equation for  $S$ . With this  $t_P$  the 3-D coordinates of  $P$  can be found by substituting  $t_P$  into  $\overrightarrow{CQ}$ .

#### B1.1 Calculation of $\overrightarrow{OP'}$

The IM coordinates  $x_{IM_{P'}}$  and  $y_{IM_{P'}}$  of the given point  $P'$  situated in  $S'$  are used to express  $\overrightarrow{OP'}$ . From Fig. 2 in combination with Fig. A1 or Fig. A2 we see that

$$\overrightarrow{OP'} = \overrightarrow{OM'} + d_{x_{IM}}^{3-D} x_{IM_{P'}} + d_{y_{IM}}^{3-D} y_{IM_{P'}} \quad (\text{B1})$$

substitution of Eq. (A3) and Eqs. (A32)–(A33) gives

$$\begin{aligned} \overrightarrow{OP'} = & R\cos\alpha(\cos\lambda_M \cos\phi_M, \sin\lambda_M \cos\phi_M, \sin\phi_M) \\ & + (-\sin\lambda_M, \cos\lambda_M, 0)x_{IM_{P'}} \\ & + (-\cos\lambda_M \sin\phi_M, -\sin\lambda_M \sin\phi_M, \cos\phi_M)y_{IM_{P'}} \end{aligned}$$

The coordinates of  $P'$  equal the components of  $\overrightarrow{OP'}$   $= (x_{P'}^{3-D}, y_{P'}^{3-D}, z_{P'}^{3-D})$  which are given by

$$x_{P'}^{3-D} = R \cos \alpha \cos \lambda_M \cos \phi_M - (\sin \lambda_M) x_{P'}^{\text{IM}} - (\cos \lambda_M \sin \phi_M) y_{\text{IM}P'} \quad (\text{B2})$$

$$y_{P'}^{3-D} = R \cos \alpha \sin \lambda_M \cos \phi_M + (\cos \lambda_M) x_{P'}^{\text{IM}} - (\sin \lambda_M \sin \phi_M) y_{\text{IM}P'} \quad (\text{B3})$$

$$z_{P'}^{3-D} = R \cos \alpha \sin \phi_M + (\cos \phi_M) y_{\text{IM}P'} \quad (\text{B4})$$

### B1.2 The parameter representation $\overrightarrow{CQ}$

In contrast to Eq. (A5) we want to express  $\overrightarrow{CQ}$  this time relative to  $P'$ , because the IM coordinates of  $P'$  are given. The 3-D rectangular coordinates of  $P'$ , expressed in the IM coordinates  $x_{\text{IM}P'}$  and  $y_{\text{IM}P'}$ , are given by Eqs. (B2)–(B4) and come into account via  $\overrightarrow{OP'}$ .

If  $Q$  is a point situated on the line  $\overrightarrow{CP'}$  then the parameter representation of  $\overrightarrow{CQ}$  can be given with

$$\overrightarrow{CQ} = \overrightarrow{OC} + (\overrightarrow{OP'} - \overrightarrow{OC})t \quad \text{for some } t \in \mathbb{R} \quad (\text{B5})$$

with  $\overrightarrow{OC} = -\overrightarrow{OM}$  as in Eq. (A6) this becomes

$$\overrightarrow{CQ} = -\overrightarrow{OM} + (\overrightarrow{OP'} + \overrightarrow{OM})t \quad (\text{B6})$$

$$= \overrightarrow{OM}(t-1) + \overrightarrow{OP'}t \quad (\text{B7})$$

with  $\overrightarrow{OM}$  as in Eq. (A1) and the components of  $\overrightarrow{OP'}$ , equal to the coordinates of  $P'$  as in Eqs. (B2)–(B4), we get

$$\overrightarrow{CQ} = R(\cos \lambda_M \cos \phi_M, \sin \lambda_M \cos \phi_M, \sin \phi_M)(t-1) + (x_{P'}^{3-D}, y_{P'}^{3-D}, z_{P'}^{3-D})t \quad (\text{B8})$$

So the coordinates of  $Q$  on  $\overrightarrow{CQ} = (x_Q^{3-D}, y_Q^{3-D}, z_Q^{3-D})$  expressed in  $t$  are

$$x_Q^{3-D} = R(\cos \lambda_M \cos \phi_M)(t-1) + x_{P'}^{3-D}t \quad (\text{B9})$$

$$y_Q^{3-D} = R(\sin \lambda_M \cos \phi_M)(t-1) + y_{P'}^{3-D}t \quad (\text{B10})$$

$$z_Q^{3-D} = R(\sin \phi_M)(t-1) + z_{P'}^{3-D}t \quad (\text{B11})$$

with  $x_{P'}^{3-D}$ ,  $y_{P'}^{3-D}$  and  $z_{P'}^{3-D}$  as in Eqs. (B2)–(B4).

### B1.3 The equation for $S$

Because the radius of the Earth is  $R$ , the equation for the spherical Earth's surface  $S$  in  $\mathbb{R}^3$  with Eq. (C4) is

$$S: (x_P^{3-D})^2 + (y_P^{3-D})^2 + (z_P^{3-D})^2 = R^2 \quad (\text{B12})$$

### B1.4 Determining the parameter $t=t_P$ for $P$

$P$  is situated at the intersection of  $\overrightarrow{CQ}$  and  $S$ . To obtain  $t_P$  we substitute the 3-D rectangular components of  $\overrightarrow{CQ}$  given by Eqs. (B9)–(B11) with  $t=t_P$  into the plane Eq. (B12) for  $S$

$$\begin{aligned} & \left[ R(\cos \lambda_M \cos \phi_M)(t_P - 1) + x_{P'}^{3-D}t_P \right]^2 \\ & + \left[ R(\sin \lambda_M \cos \phi_M)(t_P - 1) + y_{P'}^{3-D}t_P \right]^2 \\ & + \left[ R(\sin \phi_M)(t_P - 1) + z_{P'}^{3-D}t_P \right]^2 = R^2 \end{aligned}$$

which equals

$$\begin{aligned} & R^2(\cos \lambda_M \cos \phi_M)^2(t_P - 1)^2 + \\ & 2R(\cos \lambda_M \cos \phi_M)x_{P'}^{3-D}(t_P - 1)t_P + (x_{P'}^{3-D})^2t_P^2 \\ & + R^2(\sin \lambda_M \cos \phi_M)^2(t_P - 1)^2 + \\ & 2R(\sin \lambda_M \cos \phi_M)y_{P'}^{3-D}(t_P - 1)t_P + (y_{P'}^{3-D})^2t_P^2 \\ & + R^2(\sin \phi_M)^2(t_P - 1)^2 + \\ & 2R(\sin \phi_M)z_{P'}^{3-D}(t_P - 1)t_P + (z_{P'}^{3-D})^2t_P^2 = R^2 \end{aligned}$$

the left squared trigonometric-terms sum up to one, so we get

$$\begin{aligned} & R^2(t_P - 1)^2 + \left( (x_{P'}^{3-D})^2 + (y_{P'}^{3-D})^2 + (z_{P'}^{3-D})^2 \right) t_P^2 \\ & + 2R \left( (\cos \lambda_M \cos \phi_M)x_{P'}^{3-D} + (\sin \lambda_M \cos \phi_M)y_{P'}^{3-D} \right. \\ & \left. + (\sin \phi_M)z_{P'}^{3-D} \right) (t_P - 1)t_P = R^2 \end{aligned}$$

and then

$$R^2t_P^2 - 2R^2t_P + R^2 + bt_P^2 + 2Rat_P^2 - 2Rat_P = R^2$$

with

$$a = (\cos \lambda_M \cos \phi_M)x_{P'}^{3-D} + (\sin \lambda_M \cos \phi_M)y_{P'}^{3-D} + (\sin \phi_M)z_{P'}^{3-D}$$

$$b = (x_{P'}^{3-D})^2 + (y_{P'}^{3-D})^2 + (z_{P'}^{3-D})^2$$

which equals

$$(R^2 + 2Ra + b)t_P^2 = (2R^2 + 2Ra)t_P$$

One solution  $t_P=0$  gives point  $C$ , which we are not looking for. In the other case  $t_P \neq 0$ , so we can divide by  $t_P$  and end up with

$$t_P = \frac{2R^2 + 2Ra}{R^2 + 2Ra + b} \quad (\text{B13})$$

finally we write for  $t_P$

$$t_P = \frac{2R^2 + 2Ra}{R^2 + 2Ra + (x_{P'}^{3-D})^2 + (y_{P'}^{3-D})^2 + (z_{P'}^{3-D})^2} \quad (\text{B14})$$

with

$$a = (\cos\lambda_M \cos\phi_M)x_{P'}^{3-D} + (\sin\lambda_M \cos\phi_M)y_{P'}^{3-D} + (\sin\phi_M)z_{P'}^{3-D} \quad (\text{B15})$$

### B1.5 The 3-D rectangular coordinates of $P$

The 3-D rectangular coordinates of  $P$  can be obtained by taking  $t=t_P$  in Eqs. (B9)–(B11) for the components of  $\vec{CQ}$ . So the coordinates of  $P$  can be given by

$$x_P^{3-D} = R(\cos\lambda_M \cos\phi_M)(t_P - 1) + x_{P'}^{3-D} t_P \quad (\text{B16})$$

$$y_P^{3-D} = R(\sin\lambda_M \cos\phi_M)(t_P - 1) + y_{P'}^{3-D} t_P \quad (\text{B17})$$

$$z_P^{3-D} = R(\sin\phi_M)(t_P - 1) + z_{P'}^{3-D} t_P \quad (\text{B18})$$

with  $t_P$  as in Eq. (B14)

$$t_P = \frac{2R^2 + 2Ra}{R^2 + 2Ra + (x_{P'}^{3-D})^2 + (y_{P'}^{3-D})^2 + (z_{P'}^{3-D})^2} \quad (\text{B19})$$

with  $a$  as in Eq. (B15)

$$a = (\cos\lambda_M \cos\phi_M)x_{P'}^{3-D} + (\sin\lambda_M \cos\phi_M)y_{P'}^{3-D} + (\sin\phi_M)z_{P'}^{3-D} \quad (\text{B20})$$

with  $x_{P'}^{3-D}$ ,  $y_{P'}^{3-D}$  and  $z_{P'}^{3-D}$  as in Eqs. (B2)–(B4)

$$x_{P'}^{3-D} = R \cos\alpha \cos\lambda_M \cos\phi_M - (\sin\lambda_M)x_{\text{IM}P'} - (\cos\lambda_M \sin\phi_M)y_{\text{IM}P'} \quad (\text{B21})$$

$$y_{P'}^{3-D} = R \cos\alpha \sin\lambda_M \cos\phi_M + (\cos\lambda_M)x_{\text{IM}P'} - (\sin\lambda_M \sin\phi_M)y_{\text{IM}P'} \quad (\text{B22})$$

$$z_{P'}^{3-D} = R \cos\alpha \sin\phi_M + (\cos\phi_M)y_{\text{IM}P'} \quad (\text{B23})$$

### B2 The inverse projected $\lambda_P$

Considering the positive and negative values of the coordinates of  $P$  in the different quadrants the  $\lambda_P$  can be determined. The  $\lambda_P$  for an arbitrary point  $P$ , inverse projected from a point  $P'$  in  $S'$  to  $S$ , is given by

$$\left. \begin{aligned} \lambda_P &= 180^\circ + \frac{180}{\pi} \arctan \frac{y_P^{3-D}}{x_P^{3-D}} && x_P^{3-D} < 0 \\ \lambda_P &= \frac{180}{\pi} \arctan \frac{y_P^{3-D}}{x_P^{3-D}} && x_P^{3-D} > 0 \ \& \ y_P^{3-D} \geq 0 \\ \lambda_P &= 360^\circ + \frac{180}{\pi} \arctan \frac{y_P^{3-D}}{x_P^{3-D}} && \text{for } x_P^{3-D} > 0 \ \& \ y_P^{3-D} < 0 \\ \lambda_P &= 90^\circ && x_P^{3-D} = 0 \ \& \ y_P^{3-D} > 0 \\ \lambda_P &= 270^\circ && x_P^{3-D} = 0 \ \& \ y_P^{3-D} < 0 \\ \lambda_P &= 0^\circ && x_P^{3-D} = 0 \ \& \ y_P^{3-D} = 0 \end{aligned} \right\} \quad (\text{B24})$$

with  $x_P^{3-D}$  and  $y_P^{3-D}$  as in Eqs. (B16) and (B17).

### B3 The inverse projected $\phi_P$

And the  $\phi_P$  for the arbitrary point  $P$ , inverse projected from a point  $P'$  in  $S'$  to  $S$ , is given by

$$\left. \begin{aligned} \phi_P &= \frac{180}{\pi} \arctan \frac{z_P^{3-D}}{\sqrt{x_P^{3-D} + y_P^{3-D}}} && x_P^{3-D} \neq 0 \ \text{or} \ y_P^{3-D} \neq 0 \\ \phi_P &= 90^\circ && \text{for } x_P^{3-D} = y_P^{3-D} = 0 \ \& \ z_P^{3-D} > 0 \\ \phi_P &= -90^\circ && x_P^{3-D} = y_P^{3-D} = 0 \ \& \ z_P^{3-D} < 0 \end{aligned} \right\} \quad (\text{B25})$$

with  $x_P^{3-D}$ ,  $y_P^{3-D}$  and  $z_P^{3-D}$  as in Eqs. (B16)–(B18). We omitted the trivial case  $x_P^{3-D} = y_P^{3-D} = z_P^{3-D} = 0$ .

## Appendix C

### Some basic geometrical math

Points lying on the surface of an arbitrary sphere  $K$  with radius  $R_K$  can be described in geographical coordinates in  $\mathbb{R}^3$  with  $\lambda$ ,  $\phi$  and  $r$ :

$$K : (\lambda, \phi, r) = (\lambda, \phi, R_K) \quad (\text{C1})$$

The same sphere  $K$  described in rectangular cartesian coordinates  $x^{3-D}$ ,  $y^{3-D}$  and  $z^{3-D}$  in  $\mathbb{R}^3$  can be expressed in terms of the 3-D spherical angle coordinates and the radius  $R_K$  of sphere  $K$  (see Fig. 1):

$$K : (x^{3-D}, y^{3-D}, z^{3-D}) = R_K (\cos\lambda \cos\phi, \sin\lambda \cos\phi, \sin\phi) \quad (\text{C2})$$

If  $L$  is a plane in  $\mathbb{R}^3$  with a normal vector  $N=(n_x, n_y, n_z)$  in rectangular coordinates in  $\mathbb{R}^3$ , then plane  $L$  in  $\mathbb{R}^3$  can be given by the equation

$$L : n_x x^{3-D} + n_y y^{3-D} + n_z z^{3-D} = k \quad \text{for some } k \in \mathbb{R} \quad (\text{C3})$$

The equation for a sphere with radius  $R_K$  is

$$x^2 + y^2 + z^2 = R_K^2 \quad \text{for } (x, y, z) \in \mathbb{R}^3 \quad (\text{C4})$$

Two trigonometric summation rules we will use are

$$\cos(a)\cos(b) + \sin(a)\sin(b) = \cos(a-b) = \cos(b-a) \quad (\text{C5})$$

$$\sin(a)\cos(b) - \cos(a)\sin(b) = \sin(a-b) = -\sin(b-a) \quad (\text{C6})$$

*Acknowledgements.* We thank J. Ettema for providing the recent RACMO data of Greenland, and we thank W. J. van de Berg for providing the RACMO data of Antarctica. This work was funded in the framework of the Utrecht Centre for Geosciences (UCG) program. We thank D. Roche and an anonymous referee for their comments and suggestions, both the manuscript and the OBLIMAP package have benefited from them.

Edited by: C. Ritz

## References

- Bamber, J., Layberry, R., and Gogenini, S.: A new ice thickness and bed data set for the Greenland ice sheet 1: Measurement, data reduction, and errors, *J. Geophys. Res.*, 106(D24), 33781–33788, 2001.
- Bamber, J. L., Gomez-Dans, J. L., and Griggs, J. A.: A new 1 km digital elevation model of the antarctic derived from combined satellite radar and laser data 2013 part 1: Data and methods, *The Cryosphere*, 3(1), 101–111, 2009.
- Collins, W. D., Blackmon, M. L., Bonan, G. B., Hack, J. J., Henderson, T. B., Kiehl, J. T., Large, W. G., McKenna, D. S., Bitz, C. M., Bretherton, C. S., Carton, J. A., Chang, P., Doney, S. C., Santer, B. D., and Smith, R. D.: The Community Climate System Model Version 3 (CCSM3), *J. Climate*, 19, 2122–2143, 2005.
- DeConto, R. and Pollard, D.: Rapid Cenozoic glaciation of Antarctica induced by declining atmospheric CO<sub>2</sub>, *Nature*, 421, 245–249, 2003.
- Ettema, J., van den Broeke, M. R., van Meijgaard, E., van de Berg, W. J., Bamber, J. L., Box, J. E., and Bales, R. C.: Higher surface mass balance of the Greenland ice sheet revealed by high-resolution climate modeling, *Geophys. Res. Lett.*, 36, L12501, doi:10.1029/2009GL038110, 2009.
- Fabre, A., Ramstein, G., Ritz, C., Pinot, S., and Fournier, N.: Coupling an AGCM with an ISM to Investigate the Ice Sheets Mass Balance at the Last Glacial Maximum, *Geophys. Res. Lett.*, 25, 531–534, 1998.
- Fichefet, T., Poncin, C., Goosse, H., Huybrechts, P., Janssens, I., and Treut, H. L.: Implications of changes in freshwater flux from the Greenland ice sheet for the climate of the 21st century, *Geophys. Res. Lett.*, 30(17), 1911, doi:10.1029/2003GL017826, 2003.
- Huybrechts, P., Payne, A., and Group, E. I.: The EISMINT benchmarks for testing ice-sheet models, *Ann. Glaciol.*, 23, 1–12, 1996.
- Huybrechts, P., Janssens, I., Poncin, C., and Fichefet, T.: The response of the Greenland ice sheet to climate changes in the 21st century by interactive coupling of an AOGCM with a thermomechanical ice sheet model, *Ann. Glaciol.*, 35(1), 409–415, 2002.
- Huybrechts, P., Gregory, J., Janssens, I., and Wild, M.: Modelling Antarctic and Greenland volume changes during the 20th and 21st centuries forced by GCM time slice integrations, *Global Planet. Change*, 42, p. 105, 2004.
- Lythe, M. B., Vaughan, D. G., and the BEDMAP Consortium: BEDMAP: A new ice thickness and subglacial topographic model of Antarctica, *J. Geophys. Res.*, 106(B6), 11335–11351, 2001.
- Mikolajewicz, U., Vizcaíno, M., Jungclaus, J., and Schurgers, G.: Effect of ice sheet interactions in anthropogenic climate change simulations, *Geophys. Res. Lett.*, 34, L18706, doi:10.1029/2007GL031173, 2007.
- Pattyn, F.: A new three-dimensional higher-order thermomechanical ice sheet model: Basic sensitivity, ice stream development, and ice flow across subglacial lakes, *J. Geophys. Res.*, 108(B8), 2382, doi:10.1029/2002JB002329, 2003.
- Payne, A., Huybrechts, P., Abe-Ouchi, A., Calov, R., Fastook, J., Greve, R., Marshall, S., Marsiat, I., Ritz, C., Tarasov, L., and Thomassen, M.: Results from the EISMINT model intercomparison: the effects of thermomechanical coupling, *J. Glaciol.*, 46(153), 227–238, 2000.
- Reerink, T. J., van de Wal, R. S. W., and Borsboom, P.-P.: Derivation of a numerical solution of the 3D coupled velocity field for an ice sheet - ice shelf system, incorporating both full and approximate stress solutions, *Geosci. Model Dev. Discuss.*, 2, 81–158, 2009.
- Ridley, J., Huybrechts, P., Gregory, J., and Lowe, J.: Elimination of the Greenland Ice Sheet in a high CO<sub>2</sub> climate, *J. Climate*, 18(17), 3409–3427, 2005.
- Rutt, I. C., Hagdorn, M., Hulton, N. R. J., and Payne, A. J.: The glimmer community ice sheet model, *J. Geophys. Res.*, 114, F02004, doi:10.1029/2008JF001015, 2009.
- Shepard, D.: A two-dimensional interpolation function for irregularly-spaced data, *Proceedings-1968 ACM National Conference*, 517–524, 1968.
- Snyder, J. P.: Map projections: A working manual, available at: <http://pubs.er.usgs.gov/usgspubs/pp/pp1395>, Tech. rep., USGS Professional Paper 1395, ix, 385 p, 1987.
- Van de Berg, W. J., van den Broeke, M. R., Reijmer, C. H., and van Meijgaard, E.: Reassessment of the Antarctic surface mass balance using calibrated output of a regional atmospheric climate model, *J. Geophys. Res.*, 111, D11104, doi:10.1029/2005JD006495, 2006.
- Van de Berg, W. J., van den Broeke, M. R., and van Meijgaard, E.: Heat budget of the East Antarctic lower atmosphere derived from a regional atmospheric climate model, *J. Geophys. Res.*, 112, D23101, doi:10.1029/2007JD008613, 2007.
- Van de Wal, R. S. W., Wild, M., and de Wolde, J. R.: Short-term volume changes of the Greenland ice sheet in response to doubled CO<sub>2</sub> conditions, *Tellus B*, 53, 94–102, 2001.
- van Meijgaard, E., van Ulft, L., Van de Berg, W., Bosveld, F., Van den Hurk, B., Lenderink, G., and Siebesma, A.: The KNMI regional atmospheric climate model RACMO version 2.1, Tech. Rep. 302, KNMI, De Bilt, the Netherlands, 2009.
- Vizcaíno, M., Mikolajewicz, U., Groeger, M., Maier-Reimer, E., Schurgers, G., and Winguth, A.: Long-term ice sheet-climate interactions under anthropogenic greenhouse forcing simulated with a complex Earth System Model, *Clim. Dynam.*, 31(6), 665–690, 2008.